Sheffield Hallam University

Seismic collapse of self-centering steel MRFs with different column base structural properties.

KAMPERIDIS, Vasileios C <http://orcid.org/0000-0003-4893-7110>, PAPAVASILEIOU, Georgios, KAMARIS, George S and VASDRAVELLIS, George

Published version

Copyright and re-use policy

Seismic collapse of self-centering steel MRFs with different column base structural properties

Vasileios C. Kamperidis[a][1], Georgios S. Papavasileiou[b], George S. Kamaris[c] and George Vasdravellis[d]

[a]School of Applied Sciences, Abertay University, Bell Street, Dundee, DD1 1HG, UK

[b]School of Architecture and Built Environment, University of Wolverhampton, Wulfruna Street, Wolverhampton, WV1 1LY, UK

[c]Department of Civil Engineering, Liverpool John Moores University, Liverpool, L3 3AF, UK

[d]Institute for Infrastructure and Environment, Heriot-Watt University, Edinburgh, EH14 4AS, UK

ABSTRACT

The effect of the strength and stiffness characteristics of a previously proposed novel column base on the seismic performance and collapse capacity of steel self-centering moment-resisting frames is evaluated in this paper. This is done through three normalised parameters that represent the initial stiffness, post-yield stiffness, and strength of the column base, which can be independently adjusted. For these evaluations, a prototype steel building, which serves as a case study, is designed with sixteen different cases of a self-centering moment-resisting frame with different column base stiffness and strength characteristics (SC-MRF-CBs). A self-centering moment-resisting frame with conventional column bases and the same members and beam-column connections as those of the SC-MRF-CBs, named SC-MRF, serves as a benchmark frame. A set of 44 ground motions was used to conduct non-linear dynamic analyses and evaluate the seismic performance of the frames. Incremental dynamic analyses were also performed with the same ground motions set to evaluate the collapse capacity of the frames. Collapse capacity fragility curves and adjusted collapse margin ratios of the frames were derived and used for the comparison of the seismic risk of the frames. The results show

---

[1] Corresponding author, E-mail address: Vasileios.C.Kamperidis@gmail.com, ORCID ID number: 0000-0003-4893-7110.

30   that the new self-centering column base significantly improves the seismic performance of the

31   SC-MRF, demonstrating the potential of the SC-MRF-CBs to be redesigned with smaller

32   member sections. Moreover, the SC-MRF-CBs achieve significant reduction in collapse risk

33   compared to the SC-MRF. Finally, the results show that increasing the base strength and

34   stiffness improves the seismic performance and collapse capacity of the SC-MRF-CBs.

35   **KEYWORDS**

36   Column base; Self-centering; Collapse risk; Interstorey drifts and floor accelerations;

37   Parametric investigation; Seismic resilience

38   **1   INTRODUCTION**

39   Column bases have a very important role in the seismic response of steel moment-resisting

40   frames (MRFs) [1–5]. Eurocode 8 (EC8) [6] assumes that plastic hinges at the column base

41   connection will offer increased rotational ductility compared to other plasticity mechanisms

42   therein [7], such as column member plastic hinging. This strength-related code presumption

43   has been questioned by Lignos and Krawinkler [8], who showed that the ductility of the column

44   base plastic hinges may be compromised by local instabilities, leading to premature column

45   failure. Moreover, Aviram et al. [5] and Ruiz-García and Kanvinde [3] showed that decreasing

46   the initial stiffness of the base connections in low-rise buildings can change the height-wise

47   drift distribution, leading to drift and damage concertation and eventually to collapse. Zareian

48   and Kanvinde [2] showed that reducing the base fixity in low- to high-rise buildings can

49   increase the members' force demands, alter the global plastic mechanism, and significantly

50   reduce ductility, strength and collapse resistance. Torres-Rodas et al. [4] showed that increasing

51   the base flexibility of three-dimensional framed buildings, increases their transient drifts and

52   probabilities of collapse, while appreciably decreases their overstrength and ductility.

53   To address the deficiencies of MRFs under earthquakes, the self-centering MRFs (SC-MRFs)

54   were developed, such as those, for example, proposed in [9–16]. The main practice for SC-

55   MRFs is to use post-tensioned (PT) beam-column connections that utilise high-strength steel

56   tendons to clamp the beams to the columns and, thus, provide a re-centering mechanism that

57   can restore the initial geometry of the building up to a targeted seismic intensity. High-strength

58   steel is used to ensure that the tendons remain elastic up to the targeted frame response.

59   Therefore, in these SC-MRFs, the self-centering mechanism is provided through attaining a

60   targeted elastic elongation capacity for their PT tendons. Other researchers [17,18] have

61   provided self-centering mechanisms for their seismic-resilient MRFs by relying on fully

62   recoverable plastic deformations for the self-centering components of their systems up to as

63   targeted response level to eliminate the need for repair, i.e., by utilising superelastic shape

64   memory alloys (SMAs) for their self-centering components. The SC-MRFs with high-strength

65   PT tendons, which are of interest in this work, utilise energy dissipating devices (EDs) in their

66   PT beam-column connections to dissipate seismic energy and reduce the seismic forces and

67   accelerations [9]. These EDs can be easily removed or replaced, if damaged, which can

68   improve building's resilience [19,20]. Combining these techniques, SC-MRFs can minimize

69   damage and residual drifts [10] and reduce peak drifts and floor accelerations [9,21].

70   Self-centering systems can offer an option of tuning the structural properties that fully define

71   their seismic hysteretic response. These properties are the initial stiffness, post-yield stiffness,

72   strength and energy dissipation. Different researchers have evaluated the effect of these

73   properties on the seismic response of different types of self-centering systems. Christopoulos

74   et al. [22,23] concluded that if adequate energy dissipation is provided in SDOF flag-shaped

75   response systems, these could have similar or improved peak drift response compared to that

76   of elastoplastic systems of the same initial stiffness and strength. It was highlighted, though,

77   that systems with self-centering response are prone to increased resonance vibration amplitudes

78   when their post-yield stiffness ratio, α (i.e., the ratio of the post-yield stiffness over the initial

79   stiffness), is increased [23]. Subsequently, Christopoulos et al. [24] found that the maximum

80   drift response of SDOF systems with self-centering response under the design basis earthquake

81   (DBE) [6] slightly decreases for increasing values of their post-yield stiffness. Interestingly,

82   this effect was reversed for the collapse prevention seismic performance level – a finding

83   fundamentally opposite to what applies in elastoplastic systems. Karavasilis and Seo [25]

84   concluded that increasing the strength and adding damping in self-centering SDOF systems,

85   generally decreases their peak total accelerations and displacements. In contrast, Cimellaro

86   [26] suggested that the drift response of a structure may be improved by adopting lower lateral

87   strength combined with higher damping ratios. Chou and Chen [27] investigated the

88   performance of SC-MRFs with either fixed or self-centering column bases under the DBE and

89   maximum considered earthquake (MCE) [28]. However, they did not assess the effect of the

90   base strength, stiffness and energy dissipation on the seismic response of their investigated

91   systems.

92   SC-MRFs with conventional column bases still cannot fully avoid structural damage and

93   residual drifts because of the plastic hinges developed at their column bases [9,10,27,29]. To

94   address this issue, SC-MRFs with self-centering column bases with replaceable/repairable EDs

95   (SC-MRF-CBs) were developed [27,29–33]. SC-MRF-CBs can eliminate damage at their

96   column bases and, thus, exhibit negligible residual drifts. Kamperidis et al. [29] have shown

97   that these systems significantly reduce the peak drifts compared to their correspondent SC-

98   MRFs, i.e., the frame with the same PT beam-column connections and same members with the

99   SC-MRF-CB, but with conventional rigid and full-strength column bases. In addition, the

100   design procedure proposed in [29] has the ability to fine-tune in a controlled manner the

101   strength, stiffness and hysteretic behaviour of a SC-MRF-CB, keeping these parameters

102   uncoupled. Thus, one can design an SC-MRF-CB adjusting these parameters in such a way that

103   its seismic response can be enhanced. However, an extensive and thorough parametric study

104   on the effects of these parameters to the seismic response of the SC-MRF-CBs is still missing.

105 Moreover, the performance-based design approach of modern structural codes [28,34]

106 mandates that buildings should be assessed against collapse as an extra measure of safety for

107 human life, on the top of satisfying the traditional force and displacement requirements of the

108 structural codes (e.g., EC8 [6]). This triggered research towards the collapse assessment of self-

109 centering systems. In line with this, Tzimas et al. [35] found that the collapse capacity of SC-

110 MRFs subjected to both far- and near-fault earthquakes, can be significantly improved by

111 adding viscous dampers. However, the collapse risk of the SC-MRF-CBs and their potential to

112 improve the collapse capacity of seismic-resistant steel buildings has never been evaluated.

113 This paper investigates the potential of SC-MRF-CBs equipped with the novel column base

114 proposed in the work of Kamperidis et al. [29] to further improve the seismic performance and

115 reduce the collapse risk of earthquake-resilient steel buildings equipped with SC-MRFs. The

116 collapse risk of these new systems has never been assessed before and, so, it is of particular

117 importance to investigate whether they attain a better or worse collapse behaviour compared to

118 the SC-MRF. By comparing both the seismic performance and collapse risk of the SC-MRF-

119 CBs with those of the SC-MRF, the performance of the former can be evaluated against all the

120 performance criteria modern structural codes demand. As such, it can be concluded whether

121 the SC-MRF-CBs can provide the potential to be designed for smaller steel members as

122 compared to those of the SC-MRF. However, the explicit consideration of an SC-MRF-CB

123 system with smaller cross-section than those of the SC-MRF is out of the scope of this work.

124 Moreover, the mainstream approach for the SC-MRFs is to be designed for similar strength

125 and initial stiffness with their correspondent conventional MRF [10,36], referred to as

126 correspondent MRF. Besides, due to the specific configuration of their PT beam-column

127 connections, SC-MRFs do not allow for flexible stiffness and strength frame adjustments. For

128 that reason, SC-MRFs are rather restricted to adhere to the above design approach. In contrast,

129 the self-centering column bases allow for the controlled adjustment of all the structural

130 properties that are necessary to fully determine their hysteretic behaviour to targeted predefined

131 levels through mathematical formulas [29]. This base structural properties' control mechanism

132 enables the adjustment of the stiffness and strength of the SC-MRF-CBs. This work thoroughly

133 and methodologically investigates for the first time the effects of all the aforementioned base

134 structural properties on the seismic performance and collapse capacity of the SC-MRF-CBs for

135 a given level of energy dissipation in their bases. The base structural properties in question are

136 the initial stiffness, post-yield stiffness, and strength, represented through three normalised

137 factors, which are described next (Section 3.1). For this scope, a prototype steel building was

138 designed that comprises different seismic-resistant frames: i.e., an SC-MRF and sixteen SC-

139 MRF-CBs with different base stiffness and strength characteristics. The frames were modelled

140 in OpenSees, where material and geometrical nonlinearities were taken into account, along

141 with strength and stiffness degradation. A set of 44 ground motions, scaled to three code-

142 prescribed seismic intensity levels [6,28], was used to conduct dynamic analyses and evaluate

143 the seismic performance of the frames. In addition, incremental dynamic analyses (IDAs) were

144 performed with the same set of ground motions to evaluate the collapse capacity of the frames.

145 The collapse capacity fragility curves and the adjusted collapse margin ratio of the frames were

146 derived and used for the comparison of the seismic risk of the frames.

147 **2   PROTOTYPE BUILDING**

148 The 5- by 3-bay, five-storey prototype steel building of [29], depicted in Figure 1, is utilised in

149 this work. Figure 1 shows the two identical braced frames in the *Y* direction and two identical

150 seismic-resistant frames in the *X* direction the building has at its perimeter. The building has

151 ductile non-structural elements and thus, the maximum interstorey drift ratio, $\theta_{s,max}$, must be

152 less than 0.75% under the frequent occurred earthquake (FOE) in accordance with EC8 [6].

153 The design spectrum of EC8 [6] with peak ground acceleration equal to 0.35g and ground type

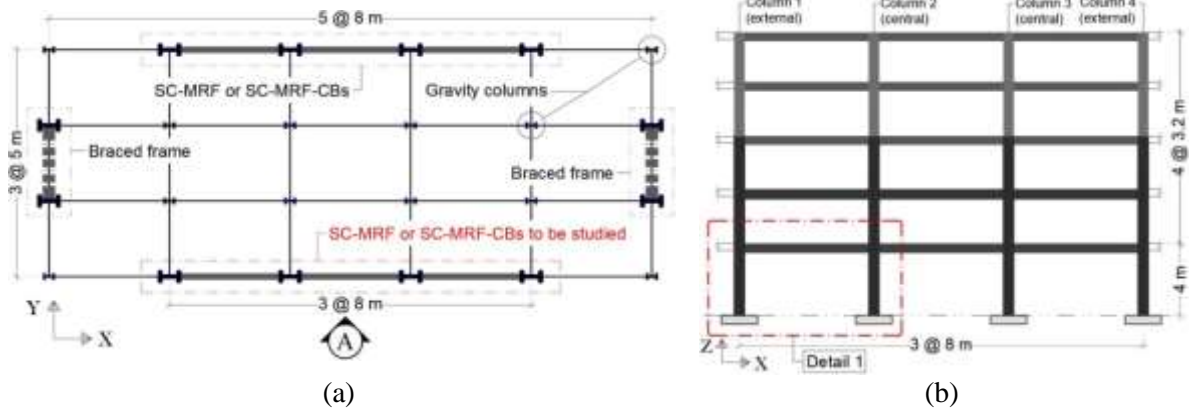154 B was used for the design of the frame under the DBE.

(a)   (b)

Figure 1 (a) Plan view; and (b) Elevation A of the prototype building.

Only the seismic-resistant frame of Elevation A of the prototype building, shown in Figure

1(b), is studied in this work. The frame of interest was designed as: (a) an SC-MRF, following

the design procedure of [10], to serve as the benchmark frame of this work; and (b) sixteen

different SC-MRF-CBs with the self-centering column bases proposed in [29], having different

base stiffness and strength characteristics but the same energy dissipation. The SC-MRF and

all SC-MRF-CBs have the same beams, columns and PT beam-column connections. The

design characteristics of the members and PT beam-column connections of the SC-MRF are

those described in [35]. Figure 2(a) illustrates the bottom-left part of an SC-MRF-CB in

Elevation A of the prototype building. The configurations of an external and internal (central)

PT beam-column connection of the frames are depicted in Figure 2(a). Figure 2(b) shows a

close-up view and the notation of these connections. The design procedure proposed in [29]

was used for the design of the self-centering column bases of the SC-MRF-CBs.

(a)   (b)

7
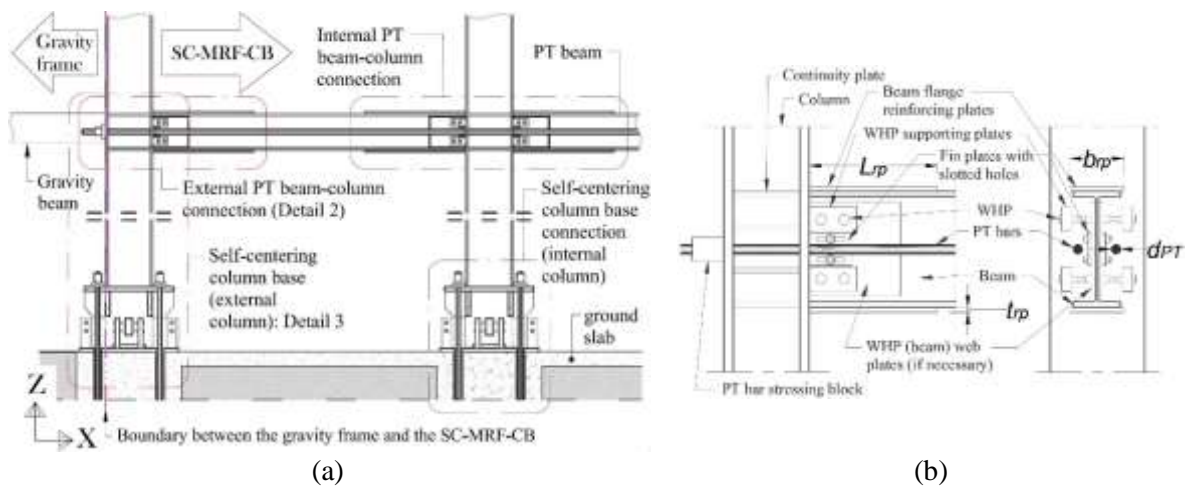
169 Figure 2 Close-up view of: (a) the bottom-left part of the SC-MRF-CB in Elevation A of the prototype
170 building (Detail 1 in Figure 1(b)); and (b) PT beam-column connection at an external column with its
171 notation (Detail 2 in Figure 2(a)).
172
173 The web hourglass pins (WHPs) described in [13] were utilised as EDs in the column bases of

174 the SC-MRF-CBs. The material of the WHPs was duplex stainless steel and its properties were

175 as follows, as per [14]: yield stress equal to 543 MPa; ultimate stress equal to 778 MPa;

176 elongation at fracture 34.25%; and Young's modulus equal to 227.848 GPa. The material for

177 the multi-wire tendons of the self-centering column bases was the low-relaxation Grade 270

178 steel material of ASTM A416 [37] with yield strength of 1676 MPa; ultimate tensile strength

179 of 1860 MPa; Young's modulus equal to 195 GPa; and ultimate elongation 3.5%. This material,

180 used in [38] and [39], is utilised in Section **Error! Reference source not found.** for the fracture

181 modelling of the tendons.

182 **3   DESIGN CASES**

183 Sixteen SC-MRF-CB design cases with different values for the strength, initial stiffness, and

184 post-yield stiffness of their self-centering column bases are employed for the parametric study

185 of this work. Thus, each self-centering column base employs a unique combination of values

186 for these three base structural properties. There are three values of strength, three values of

187 initial stiffness and five values of post-yield stiffness that are combined to form these sixteen

188 combinations in the self-centering column bases. These values cover the whole range of

189 feasible values that can be achieved each base structural property when designing the self-

190 centering column utilising the design procedure proposed in [29]. The three ranges of feasible

191 values of the base structural properties are delimited by the given column cross-section and

192 column design loads, which serve as input for the aforementioned design procedure [29]. The

193 column and its design loads are derived from the elastic analysis and design of the

194 correspondent MRF, from which the SC-MRF-CBs' designs stem [29]; this will be further

195 explained next (Section 3.2). By examining self-centering column bases with base structural

196   properties that span the whole range of their feasible values, the limits of the distinct effect of

197   each one of these properties on the seismic response and collapse capacity of the SC-MRF-

198   CBs can effectively be determined. The notation of the self-centering column bases can be seen

199   in Figure 3(a). Each self-centering column base is considered to be a cantilevered assembly

200   that comprises the self-centering low-damage column base connection, proposed in [29], and

201   the steel column member of the first storey of the frame (Figure 3(a)). The self-centering

202   column base connections are determined by the height of the concrete-filled tube (CFT) (seen

203   in Figure 3(a)), L_{CFT}. The steel columns extend from the top of their self-centering base

204   connections up to the lower limit of the panel zones of the first-storey PT beam-column

205   connections. This limit is the level of the bottom flanges of the first-storey PT beams, as

206   indicated by the red dashed line in Figure 3(a). The steel columns are determined by their

207   length, L_c, as it is shown in Figure 3(a).

(a)   (b)
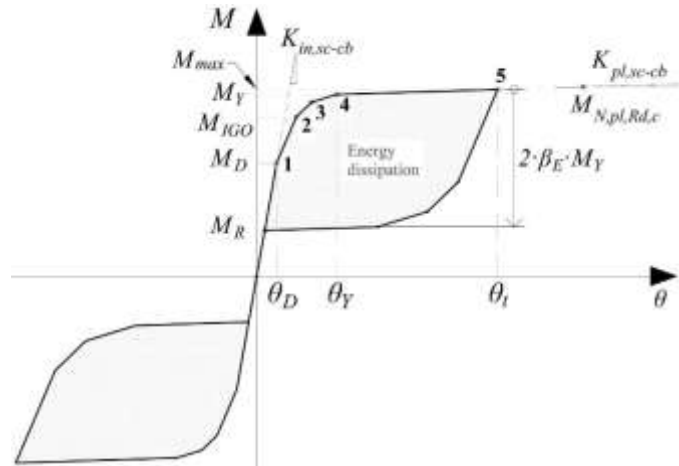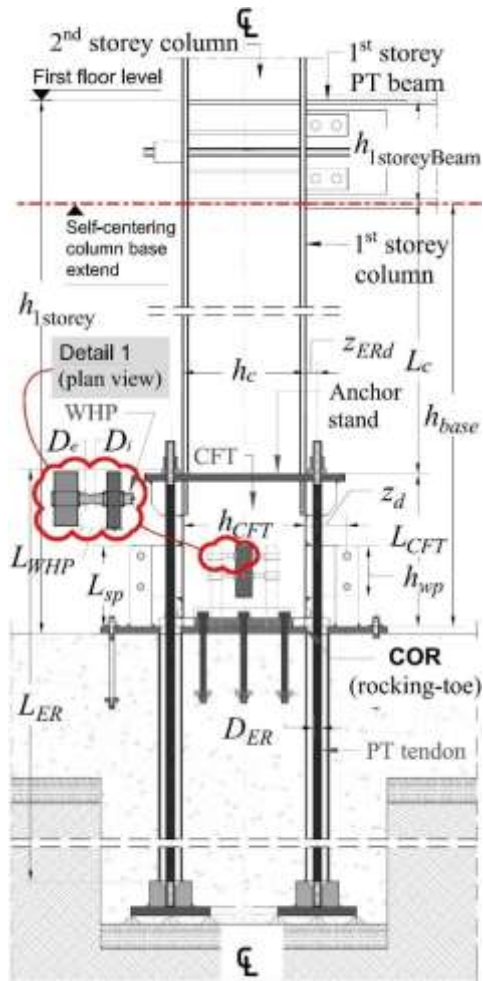
Figure 3 Self-centering column base: (a) configuration (Detail 3 in Figure 2(a)) and notation; and (b) theoretical moment (M)-rotation (θ) behaviour for an assumed clockwise bending moment and axial force.

The rationale for considering this specific cantilevered assembly configuration as the means of assessing the base stiffness and strength of the SC-MRF-CBs is that it exclusively includes the only two elements that change in the whole configuration of the SC-MRF-CBs, i.e., the base connection and its connecting steel first-storey column. All the other parts of the frames are the same as those of the SC-MRF. Similar approaches have been adopted in previous relevant research [40]. Such an approach facilitates the large computational demands of this work. The theoretical moment (M)-rotation (θ) behaviour of the self-centering column bases can be seen in Figure 3(b). In this figure, θ is the chord rotation of the self-centering column bases, defined as the lateral displacement at the top of the column divided by the total height of the column bases, h_{base}. Thus, h_{base} is related with the geometry of the frame through the following relation:

$$h_{base} = h_{1storey} - h_{1storeyBeam} \qquad (1)$$

where $h_{1storey}$ is the total height of the first storey and $h_{1storeyBeam}$ is the cross-sectional depth of the beams of the first floor.

3.1   Investigated base structural properties

The investigated structural properties of the self-centering column bases (or simply base structural properties) that are studied in this work are their strength, M_{IGO}, initial stiffness, $K_{in,sc-cb}$, and post-yield stiffness, $K_{pl,sc-cb}$, which are described in Figure 3(b). M_{IGO} is the moment at the first yielding of the WHPs of the self-centering column base connection (Figure 3(b)). M_{IGO} is considered to represent the flexural strength of the self-centering column bases because the strength of a system with metallic fuses should correspond to the point where the first yielding of its structural fuses occurs [41]. The self-centering column base allows the controlled adjustment of these base structural properties by utilising the analytical expressions that are presented next. To uncouple the research findings of this work from the specific design characteristics of the frames studied herein (e.g., the size of the first-storey columns, the cross-sectional depth of which, denoted as h_c (see Figure 3(a)), and its plastic moment of resistance, $M_{N,pl,Rd,c}$ (described in Eq. (3), below), are of interest in this study), the base structural properties are represented by the following normalised parameters: (a) the strength ratio, η; (b) the normalised initial base stiffness factor, β_{base}; and (c) the post-yield stiffness ratio, α. Thus, the findings of this work can be extended to any SC-MRF-CB that is designed as per the design procedure proposed in [29].

Likewise previous research [25,42], the energy dissipation factor, β_E, is utilised to control the energy dissipation in all sixteen self-centering column bases. β_E was selected to take the same, near-maximum allowable value to allow the self-centering behaviour of the column bases and maximise their seismic energy dissipation. Thus, β_E was not included in the parametric study. Based on previous relevant research [22,23,43], it was hypothesized that by maximising the

11

247 energy dissipation at the column bases, the seismic response and collapse capacity of the SC-

248 MRF-CBs would be optimally improved. Because the upper bound of β_E equals 0.5 [25,42], β_E

249 was conservatively taken equal to 0.48 in all self-centering column bases. The energy

250 dissipation in each self-centering column base is due to the energy dissipated by the WHPs up

251 to the target base rotation, θ_t (Figure 3(b)); the steel columns were intended to remain elastic

252 and not contribute to the energy dissipation of the self-centering column bases. For this

253 research, θ_t was conservatively chosen to be equal to the rotation capacity limit of EC8 for

254 ductility class high MRFs, i.e., 0.035 radians [6]. This implies that no strength and stiffness

255 deterioration was expected to take place up to θ_t. β_E was defined as:

$$\beta_E = \frac{M_Y - M_D}{M_Y} \qquad (2)$$

257 where M_Y is the moment of the self-centering column bases when all WHPs have reached their

258 elastic limit; and M_D is the decompression moment of the self-centering connection, i.e., the

259 moment at which the gap at the rocking interface of the column base opens [10,29]. These

260 characteristic moments, along with their corresponding rotations, can be seen in Figure 3(b).

261 The strength factor, η, was defined as:

$$\eta = \frac{M_{IGO}}{M_{N,pl,Rd,c}} \qquad (3)$$

263 where M_{IGO} is the moment at the first yielding of the WHPs of the self-centering column base

264 connection; $M_{N,pl,Rd,c}$ is the plastic moment of resistance of the column. $M_{N,pl,Rd,c}$ accounts for

265 interaction with the design axial force, N_{Ed}, and the overstrength of the connections materials

266 and for other material effects, in accordance with EC8 [6] and Eurocode 3 (EC3) [44]

267 provisions. N_{Ed} is the axial force derived from the analysis of the correspondent MRF for the

268 gravity loads combination of actions [29]. The strength factor η consists a measure of the

269 strength of the base connection but can represent the strength of the whole self-centering

270   column base because the former is the only part of the latter that is expected to yield up to θ_t.

271   The concept that the strength factor η consists a measure of the column bases' strength was

272   adopted on the basis that it relates the yield strength of the base connections with that of the

273   column member. This is in line with the relevant provisions of Eurocode 3 [45] that classify

274   moment-resisting connections with respect to their strength by comparing the strength of the

275   connections with the strength of their connecting members. Previous research on PT beam-

276   column connections [10] has set out an upper limit for η equal to unity. The parametric

277   investigation of this work shown that to achieve self-centering and damage-control behaviour

278   up to θ_t, only values of η below 0.45 were capable of yielding self-centering column base

279   designs with initial and post-yield stiffness within their feasible range of values; these latter

280   two base structural properties were controlled through their normalised factors, β_{base} and α,

281   respectively, described next. For that reason, the three values of η this work examined were

282   0.30, 0.35 and 0.40.

283   The normalised initial base stiffness factor, β_{base}, was defined as:

$$\beta_{base} = \frac{K_{in,sc-cb}}{K_{in,conv}} \tag{4}$$

285   where $K_{in,conv}$ is the initial (elastic) flexural stiffness of a cantilever-fixed steel column of total

286   height equal to h_{base}; and $K_{in,sc-cb}$ the initial stiffness of a self-centering column base, assumed

287   equal to the elastic flexural stiffness of the steel cantilevered column on the top of the self-

288   centering column base connection, $K_{el,col}$, since the initial stiffness of the latter connection is

289   taken as infinite [29]. Thus, $K_{el,col}$ is calculated for a column height of L_c. For the self-centering

290   column bases under investigation, the three β_{base} values examined were 133%, 167% and 200%.

291   The post-yield stiffness ratio, α, was defined according to the following relation:

$$\alpha = \frac{K_{pl,sc-cb}}{K_{in,sc-cb}} \quad (5)$$

293   where $K_{pl,sc-cb}$ is the post-yield stiffness of the self-centering column base, defined as:

$$K_{pl,Sc-Bc} = \frac{K_{pl,sc-cb} \cdot K_{el,col}}{K_{pl,sc-cb} + K_{el,col}} \quad (6)$$

295   where $K_{pl,sc-cb}$ is the post-yield stiffness of the self-centering column base connection, which

296   was determined by the following relation [29]:

$$K_{pl,sc-cb} = K_{fe} \cdot \left(\lambda \cdot n_{WHPu} \cdot z_u^2 + \lambda \cdot n_{WHPc} \cdot z_c^2 + \lambda \cdot n_{WHPd} \cdot z_d^2 \right) + K_{ER} \cdot \left(n_{ERu} \cdot z_{ERu}^2 + n_{ERd} \cdot z_{ERd}^2 \right) \quad (7)$$

298   where k_{fe} is the elastic stiffness of a single WHP [29]; λ equals 2% according to [29]; n_{WHPu} and

299   n_{WHPd} are the numbers of the WHPs at the gap-opening and rocking-toe side of the self-

300   centering column base connections (the rocking toe coincides with the centre of rotation of the

301   connection (COR), as it is seen in Figure 3(a) for an assumed clockwise moment); n_{WHPc} the

302   number of the central WHPs; z_u, z_d and z_c, the lever arms of the WHPs at the gap-opening side,

303   rocking-toe side and that of the central WHPs, respectively; K_{ER} is the elastic axial stiffness of

304   each tendon, equal to $E_{ER} \cdot A_{ER}/L_{ER}$, with E_{ER}, A_{ER} and L_{ER} the tendon's material Young's

305   modulus, cross-sectional area and length, respectively; and n_{ERu} and n_{ERd}, and z_{ERu} and z_{ERd} the

306   number and lever arms of the PT tendons at the gap-opening and rocking-toe side of the self-

307   centering column base, respectively. The lever arms z_d and z_{ERd}, are defined in Figure 3(a). The

308   lever arms z_u and z_{ERu} were derived by adding to z_d and z_{ERd} the cross-sectional depth of the

309   CFT, h_{CFT}, respectively. z_c equals $h_{CFT}/2$. Five different values of α were examined in this work,

310   i.e., 5%, 10%, 15%, 20% and 24.5%. The value of 24.5% was the maximum value of α obtained

311   for the given level of strength and initial stiffness of the relevant self-centering column base.

312   This is in agreement with the maximum achievable limit of α for real flag-shaped response

313   systems, determined to about 25%, proposed by Wiebe and Christopoulos [46].

314   *3.2   Self-centering column base design procedure*

315   This section presents the design procedure utilised to derive the sixteen self-centering column

316   base designs that are investigated in this work. The design procedure is that described in the

317   work of Kamperidis et al. [29], with the only difference being that – in this work – the

318   investigated base structural properties are given pre-selected values utilising Eq. (2) through

319   (7) of Section 3.1. Pre-selecting these values, reduces the number of unknowns to be

320   determined (as compared to the approach adopted in [29]), significantly facilitating the design

321   process. To minimize repetition since the design procedure in [29] has been presented therein

322   in detail, the design approach adopted in this work presents only limited mathematical formulas

323   from [29].

324   To initiate the design procedure, the following input quantities are required: the column axial

325   force, N_{Ed}; the column cross-section, so that its cross-sectional depth, h_c, and plastic moment

326   of resistance, $M_{N,plRd,c}$, are determined; and the target base rotation, θ_t. The design procedure

327   comprises the following steps:

328   Step 1: Design the tendons

329   (a) Select a value for β_{base} and calculate $K_{in,sc-cb}$ from Eq. (4). From $K_{in,sc-cb}$, L_c is derived

330   utilising the relevant elastic flexural stiffness formula from mechanics (Section 3.1).

331   From Figure 3(a) and given the resulted L_c value, h_{CFT} can be derived.

332   (b) Select a value for the strength factor, η. From Eq. (3) M_{IGO} can then be derived.

333   (c) Select a value for the ratio M_D/M_{IGO} so that is it larger than 0.5, but as closer as it gets

334   to that latter value. This is to ensure self-centering capability but also to maximize

335   energy dissipation. Thus, M_D is derived.

336   (d) Select a number, $n_{ERu}=n_{ERd}$, and a lever arm for the tendons, e.g., z_{ERd} (z_{ERu} can be

337   determined as per Section 3.1). It is suggested that four tendons are placed at the corners

338   of the anchor stand, which is the elevated stiff plate welded on the top of the CFT (see

339   Figure 3(a)); i.e., $n_{ERu}=n_{ERd}=2$. Then, calculate the initial post-tensioning force at each

340   tendon, T, as per Eq. (2) of Kamperidis et al. [29].

341 (e) Select an appropriate high-strength steel grade material for the tendons, e.g., Grade 270

342   steel material of ASTM A416, to ensure a high yield strength, $f_{y,ER}$, for the tendons, and

343   assume a diameter for them, D_{ER} (this determines A_{ER}). Then, utilize Eq. (3) of [29] to

344   calculate L_{ER}. Also, approximate the moment contribution of the tendons for the

345   characteristic rotation, θ_2, denoted as $M_{ER}(\theta_2)$, as per Eq. (7) of [29]. θ_2 is the rotation

346   at which the first WHP of the self-centering column base yields. $M_{ER}(\theta_2)$ is to be used

347   next.

348 Step 2: Design the WHPs

349 (a) Select a number for the WHPs at each side of the self-centering column base (e.g.,

350   n_{WHPd}). It is suggested that two WHPs are placed at all sides of the column base; this is

351   for construction practicality and to ensure that the column base control its structural

352   properties over both of its main axes [29]; i.e., $n_{WHPd}= n_{WHPc}= n_{WHPu}= 2$. Also, select a

353   lever arm for the WHPs, e.g., z_d (z_u and z_c can be determined as per Section 3.1). Then,

354   calculate the yield strength of a single WHP, $F_{y,WHPi}$, as per Eq. (5) of [29], utilising

355    $M_{ER}(\theta_2)$ from Step 1(e). The internal diameter of the WHPs, D_i (described in Detail 1

356   of Figure 3(a)), can then be calculated from the following relation as per [10,29]:

357
$$D_i = \sqrt{\frac{2 \cdot F_{y,WHP,i} \cdot \sqrt{3}}{\pi \cdot f_{y,WHP}}}\qquad(8)$$

358   where $f_{y,WHP}$ is the yield strength of the material of the WHPs.

359 (b) Select a value for α, and based on Eq. (5) and the value of $K_{in,sc-cb}$ derived from Step

360   1(a), calculate $K_{pl,sc-cb}$. Based on the $K_{pl,sc-cb}$ value, calculate the WHPs' elastic stiffness

361   K_{fe} from Eq. (7). Moreover, to derive a relationship between the length of the tapered

362   part of half a WHP, L_{WHP}, and the external diameter of the WHP, D_e, substitute D_i from

363   Eq. (8) into the following relationship [29,47]:

364
$$L_{WHP} = \frac{2.566 \cdot D_e^3}{\pi \cdot D_i^2} \tag{9}$$

365   Both L_{WHP} and D_e are described in Detail 1 of Figure 3(a). A second relationship between

366   L_{WHP} and D_e, can be derived by substituting K_{fe} from above and D_i from Eq. (8) into the

367   following relationship [13,29]:

368
$$K_{fe} = 2 \cdot \frac{9 \cdot \pi \cdot D_e^3 \cdot D_i \cdot E_{WHP} \cdot G_{WHP}}{40 \cdot E_{WHP} \cdot D_e^2 \cdot L_{WHP} + 48 \cdot G_{WHP} \cdot L_{WHP}^3} \tag{10}$$

369   where E_{WHP} and G_{WHP} are the elastic and shear moduli of the WHP material. Solving the

370   system of Eqs. (9) and (10), the values of D_e and L_{WHP} can be derived.

371   Step 3: Check the self-centering capability of the column base and the column plastic hinge

372   avoidance

373   The self-centering capability of the column bases is checked by utilising Relationships (9)

374   through (11) and Relationship (17) from [29]. There are two cases:

375   (a) If self-centering behaviour is achieved, then proceed with checking whether a plastic

376   hinge is formed at the bottom of the column member. This is done by utilising

377   Relationship [20] of [29]. Two case are now identified:

378   1. A plastic hinge is formed: in this case, decrease A_{ER} in Step 1(e) by be employing a

379   smaller tendon (smaller D_{ER}), and repeat all steps up to this point until this check is

380   satisfied. Then finalize the procedure.

381   2. A plastic hinge is not formed: in this case, finalize the design process.

382   (b) If self-centering behaviour is not achieved, return to Step 1(c) and increase the ratio

383   M_D/M_{IGO}. Then, repeat the design procedure up to Step 3(a) until self-centering is

384   achieved and plastic hinge is not formed at the column. When Step 3(a) is fully

385   satisfied, complete the design process.

386   The design steps are summarized in the flowchart of Figure 4.
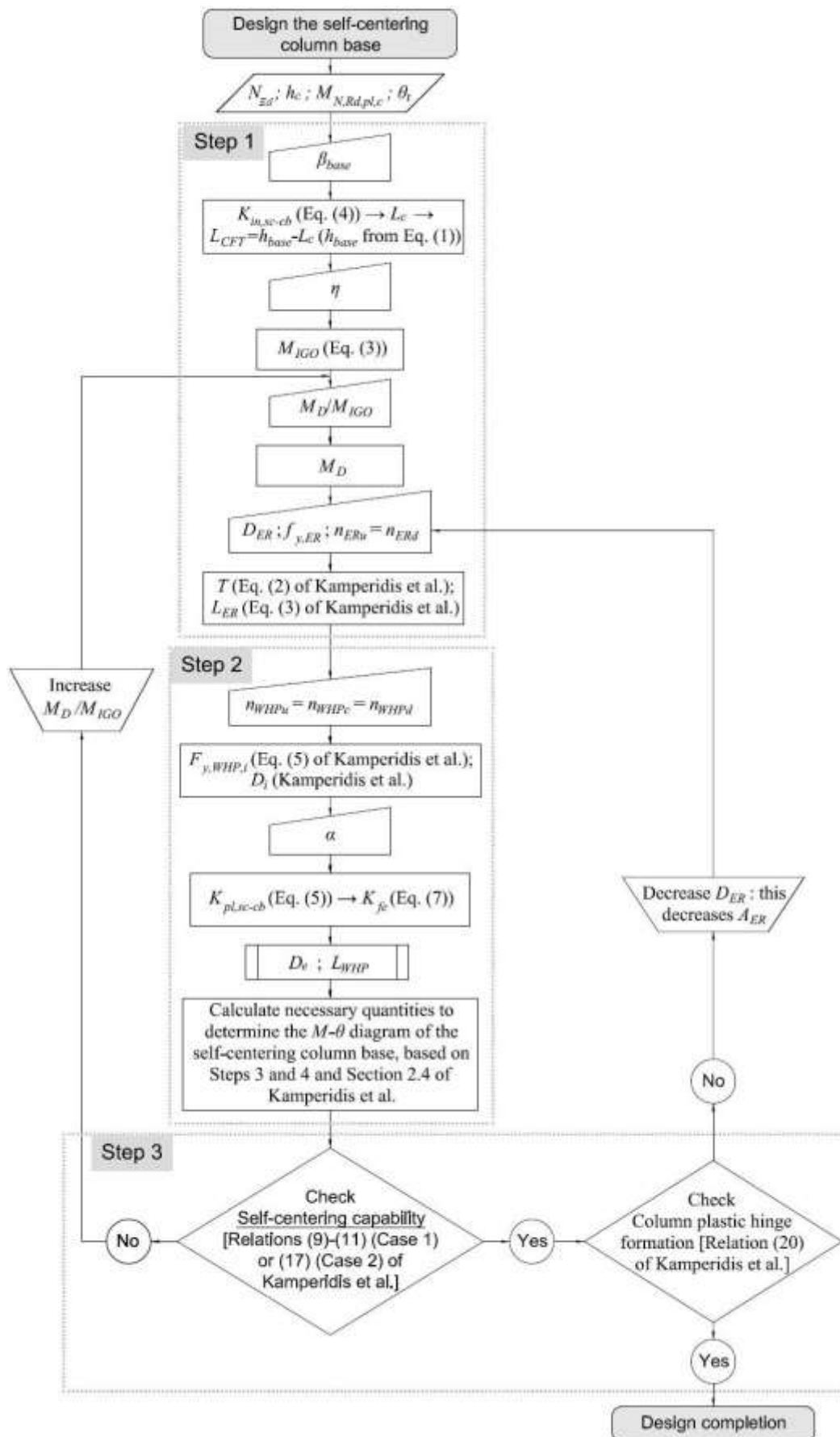
Figure 4 Flowchart of the design approach of the self-centering column bases, based on the design procedure proposed in Kamperidis et al. [29].

3.3   Self-centering column base designs

390   Table 1 lists the normalised base structural properties of the sixteen self-centering column base

391   designs and Table 2 presents their key design characteristics. These design characteristics were

392   derived utilising the design procedure presented in Section 3.2. The notation utilised in Table

393   2 is described in Figure 3(a) (and its Detail 1) and in Section 3.2.

394   Table 1. Normalised base structural properties of the sixteen self-centering column bases.

Frame	η	β_{base} (%)	α (%)
H40K133A5	0.4	133	5
H40K133A15	0.4	133	15
H40K167A15	0.4	167	15
H40K167A5	0.4	167	5
H40K133A10	0.4	133	10
H40K167A10	0.4	167	10
H40K133A24	0.4	133	24.5
H35K133A5	0.35	133	5
H35K133A15	0.35	133	15
H35K167A15	0.35	167	15
H35K167A5	0.35	167	5
H35K133A10	0.35	133	10
H35K167A10	0.35	167	10
H35K200A10	0.35	200	10
H35K133A20	0.35	133	20
H30K133A10	0.30	133	10

395

396   Table 2. Key column base design characteristics of the sixteen SC-MRF-CBs.

Frame	L_{WHP} (m)	D_e (m)	D_i (m)	$F_{y,WHP,i}$ (kN)	K_{fe} (MN/m)	L_{sp} (m)	h_{wp} (m)	L_{ER} (m)	D_{ER} (m)	z_d (m)	$z_{ER,d}$ (m)	L_{CFT} (m)	T (kN)
H40K133A5	0.12	0.04	0.02	161.78	109.22	0.37	0.24	7.49	0.02	0.24	0.09	0.44	262.70
H40K133A15	0.07	0.03	0.02	156.39	260.19	0.33	0.21	7.47	0.02	0.26	0.16	0.44	271.41
H40K167A15	0.06	0.03	0.02	158.54	307.41	0.33	0.20	7.39	0.02	0.24	0.37	0.73	273.25
H40K167A5	0.21	0.05	0.02	151.38	38.68	0.40	0.27	9.59	0.02	0.25	0.38	0.73	228.89
H40K133A10	0.06	0.04	0.02	166.28	357.10	0.33	0.20	8.50	0.02	0.21	0.15	0.44	274.02
H40K167A10	0.10	0.04	0.02	132.46	122.24	0.34	0.22	7.62	0.02	0.42	0.37	0.73	261.05
H40K133A24	0.06	0.03	0.02	163.63	396.73	0.32	0.20	5.52	0.03	0.19	0.10	0.44	281.83
H35K133A5	0.12	0.04	0.02	136.90	89.09	0.36	0.23	7.58	0.02	0.27	0.12	0.44	204.77
H35K133A15	0.06	0.04	0.02	142.89	264.52	0.32	0.20	6.64	0.02	0.22	0.16	0.44	212.16
H35K167A15	0.06	0.03	0.02	100.44	189.61	0.30	0.18	7.32	0.02	0.56	0.36	0.73	212.51
H35K167A5	0.19	0.04	0.02	125.10	34.27	0.38	0.26	8.73	0.02	0.27	0.38	0.73	171.44
H35K133A10	0.08	0.04	0.02	142.58	184.52	0.34	0.21	6.35	0.02	0.23	0.16	0.44	207.34
H35K167A10	0.05	0.04	0.02	88.76	184.92	0.30	0.17	8.65	0.02	0.70	0.36	0.73	215.25
H35K200A10	0.06	0.04	0.02	125.24	251.67	0.31	0.19	8.70	0.02	0.34	0.50	0.91	212.51
H35K133A20	0.06	0.03	0.02	113.55	252.32	0.31	0.18	7.64	0.03	0.44	0.13	0.44	212.51
H30K133A10	0.06	0.03	0.02	104.64	212.41	0.30	0.18	5.99	0.03	0.37	0.15	0.44	151.00

397

4   NON-LINEAR MODELS

399   The OpenSees platform [48] was used to model the prototype SC-MRF and SC-MRF-CBs.

400   The PT beam-column connections in all frames were modelled as in [35]. The columns and the

401   length of the beams that is reinforced were modelled with beam-column fiber elements that

402   exhibit bi-linear elastoplastic stress-strain behaviour. Force-based beam-column fiber elements

403   with end hinges [49] were used for the un-reinforced lengths of the beams. The stress-strain

404   cyclic behaviour of the fibers was modelled by utilising the modified Ibarra-Krawinkler model

405   [50]. This model was used because it captures the strength and stiffness degradation resulting

406   from beam local buckling observed after the end of the beam flange reinforcing plates. This

407   type of modelling was used in [51] and results in hysteretic curves for flexural members that

408   are smooth and similar to the ones observed in experiments. The Ibarra-Krawinkler model does

409   not take into account the effect of a variable axial force on the bending deterioration parameters

410   [51]. The use of fiber elements results in reductions of the bending strength of the beam-column

411   elements due to the variable axial-moment interaction [51]. Thus, this approach also captures

412   the axial force (caused by the PT force at the tendons) – bending moment interaction in the

413   beams of the frames [35,51]. Panel zones are modelled based on [52]. The OpenSees model

414   developed in [29] is used for the column bases of the SC-MRF-CBs. The gravity columns of

415   the tributary area of the frames are modelled as three lean-on columns to take into account P-

416   Δ effects. Truss elements that connect the nodes of the lean-on columns to nodes defined along

417   the length of the beams at the points where the secondary beams are placed are used to model

418   diaphragm action of the composite slabs. The diaphragm also helps to avoid the shortening of

419   the PT beams (as these are seen in Figure 2(a)) due to the increase of the post-tensioning forces

420   caused by to the connections' gap opening and closing during seismic loads (the PT beams are

421   only resist the constant axial force caused by the initial post-tensioning of their PT bars [10]).

422   The stiffness of these trusses is 100 times larger than that of the axial stiffness of the beam. By

423   connecting separately each bay's secondary beam nodes with the corresponding lean-on

424   column node of the same storey, these stiff truss elements help to model the discontinuity

425   between the composite slabs that correspond to each different bay of the self-centering system,

426   as per the tributary area of the bay. Discontinuity between the composite slab and the flanges

427   of the columns of the self-centering system is also assumed for the floor system utilised in this

428   work [53]. The aim of the above floor system discontinuities is to avoid that the PT beam be

429   restrained by the composite slab (minimizing the damage in the slab also); allow the free gap

430   opening and closing of the PT connection (thus, not affecting the connection's hysteretic

431   behaviour) [10,53]; and allow for the unobstructed self-centering frame expansion [10,36].

432   More details on the adopted floor system can be found in [10,53,54]. The tendons of the column

433   bases were modelled to fracture to more accurately simulate the actual collapse limit of the

434   frames under investigation. To this purpose, the Fatigue material of OpenSees [48] was utilised

435   in conjunction with the parent material of the tendons. The parent material of the tendons is the

436   material around which the Fatigue material is wrapped [48], and which in this case is the

437   material steel01 of OpenSees [48]. The material steel01 has a bilinear elastoplastic hysteresis

438   with post-stiffness ratio equal to 0.03 [29]. The Fatigue material is wrapped around the steel01

439   material without altering the stress-strain relationship of the latter [48]. The Fatigue material

440   utilises the Coffin-Manson relationship [55] and the Palmgren-Miner linear damage

441   accumulation rule [55] to model their low-cycle fatigue and fracture. The Coffin-Manson rule

442   is expressed by the relationship:

443
$$\frac{\Delta\varepsilon_p}{2} = \varepsilon_f' \cdot \left(2 \cdot N_f\right)^m \tag{11}$$

444   where $\frac{\Delta\varepsilon_p}{2}$ is the plastic strain amplitude; ε_f' the fatigue ductility coefficient, which represents

445   the intersect of the plastic asymptotic line of the Coffin-Manson curve in the log-log space, i.e.,

446   the strain at which one cycle will cause failure (fracture) [55,56]; N_f the number of the full

447   cycles to failure (or $2 \cdot N_f$ the number of load reversals to failure); and m the fatigue ductility

448   exponent, which represents the sensitivity of the log of the strain amplitude to the log of N_f

449   [56], i.e., the slope of the Coffin-Manson curve in the log-log space. For the Fatigue material

450   of the tendons, ε_f' was taken equal to 4%. This strain value is a conservative fracture value as:

451   (a) it represents the initial wire fracture of the strands of the tendons, ignoring the appreciable

452   strength reserve that remains at the tendons afterwards and through the fracture of all their

453   wires [38,39]; (b) it considers the premature fracture of the tendons due to excessive stress

454   concentration at the vicinity of their anchors, as per the work of Bruce and Eatherton [38],

455   where the fracture value in question represents the average observed first-wire fracture limit

456   (not the relevant proposed design limit) from their tested specimens, considering both the

457   tendon materials used therein, and also a newer multiple-use barrel and wedge anchorage

458   system that allowed for larger inelastic strains prior to initial wire fracture, compared to the

459   traditional barrel and wedge anchorage system that the authors also tested in their work; (c) it

460   represents the upper first-wire fracture limit attained from the tested specimens in the work of

461   Sideris et al. [39], given that their observed strain fracture values ranged from 1.5% to 4%; and

462   (d) it is a value much smaller than those provided by these tendons manufacturers, i.e., 6-7%

463   [57]. The fatigue ductility exponent, m, for the Fatigue material of OpenSees, was taken equal

464   to -0.458, as per the work of Uriz [56]. For the maximum values of strain to be set out in the

465   model of the material, the suggested minimum and maximum values of -1e16 and 1e16,

466   respectively, have been adopted [48]. To accumulate damage in the material due to the random

467   strain amplitude excursions during an earthquake, the Fatigue material of OpenSees utilises a

468   rainflow method [55] counting algorithm to count the number of cycles at various strain

469   amplitudes, in conjunction with the Palmgren-Miner's linear damage accumulation Rule [55].

470   The Palmgren-Miner's Rule is expressed by the damage index, D, which is given by the

471   following mathematical formula:

23

$$472 \qquad\qquad\qquad\qquad D = \sum_{i=1}^{j} \frac{n_i}{N_{f,i}} \qquad\qquad\qquad\qquad (12)$$

473   where $N_{f,i}$ is the number of cycles that can be resisted by the material until failure at the ith

474   constant strain amplitude loading, in a total of j such loadings with constant strain amplitudes;

475   and n_i is the number of loading cycles the material has undergone at the ith constant strain

476   amplitude loading [55]. Once index D in the Fatigue material reaches the value of 1.0, the force

477   (or stress) in the parent material becomes zero, signalling the failure of the parent material [48].

478   The fracture of the WHPs was not modelled in this study, as, based on previous experimental

479   and numerical studies [14,54,58], their geometry and position around the column bases can be

480   selected to avoid fracture before the building's seismic collapse due to second order effects

481   [51].

482   **5   NON-LINEAR DYNAMIC ANALYSES**

483   The set of the far-fault ground motions of FEMA P695 [59] was used for the non-linear

484   dynamic analyses of this study. This set comprises 22 record pairs, each with two horizontal

485   components for a total of 44 records. The ground motions of the above set were recorded on

486   stiff soil and at sites with distance larger than or equal to 10 km from fault rupture. The

487   magnitudes of the earthquakes range from M 6.5 to M 7.6 with an average magnitude of M 7.0.

488   The records were scaled to DBE and MCE, using as intensity measure (IM) the 5% spectral

489   acceleration at fundamental period T_1 of the frame models, $S_a(T_1)$.

490   *5.1   Assessment of the seismic performance of the frames*

491   The results of the 44 non-linear dynamic analyses for the SC-MRF and sixteen SC-MRF-CBs

492   were post-processed and the median maximum values of $\theta_{s,max}$ of all the storeys and peak floor

493   acceleration (PFA) from all the floors are shown in Table 3. The results in Table 3 indicate that

494   the $\theta_{s,max}$ of all SC-MRF-CBs is lower than that of the SC-MRF under the FOE, DBE and MCE

495   seismic intensity levels. In particular, for the FOE intensity level, the relative reduction of the

496     $\theta_{s,max}$ of the SC-MRF-CBs compared to that of the SC-MRF ranges from 3.03% for the

497   H35K167A5 to 23.65% for the H35K167A10. Under the DBE, the relevant minimum

498   reduction of $\theta_{s,max}$ is 1.42% and achieved for the H35K133A5 and the maximum is 24.13% and

499   achieved for the H40K167A15. Under the MCE, the H35K133A5 achieves the minimum

500   reduction of $\theta_{s,max}$ equal to 0.95% and the H35K167A10 the maximum equal to 18.55%.

501   Moreover, all the SC-MRF-CBs achieve $\theta_{s,max}$ lower than the "life safety" and "collapse

502   prevention" limits of EC8 [6] and ASCE/SEI 41-06 [60]. As it can be seen from Table 3, the

503   SC-MRF-CBs achieve as much as a 24.05% overall $\theta_{s,max}$ reduction (minimum reduction

504   between all seismic intensity levels for the H35K167A10). These results demonstrate that the

505   new column base configuration is very effective in reducing $\theta_{s,max}$, and that is done by only

506   adjusting its base stiffness and strength characteristics.

507
508 Table 3. Median maximum values of $\theta_{s,max}$ of all the storeys and PFA from all the floors of the SC-MRF and SC-MRF-CB design cases.
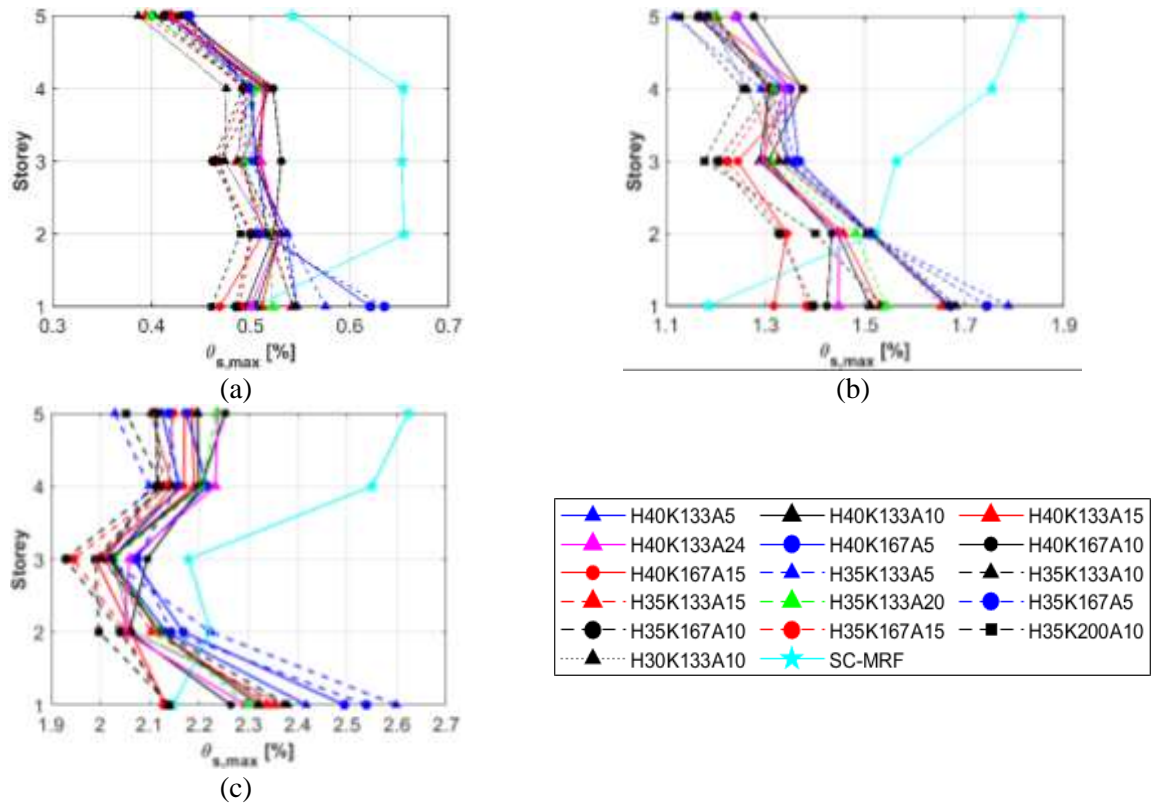
Frame	Fundamental Period T_1 (s)	$\theta_{s,max}$ (%)			PFA (g)		
		FOE	DBE	MCE	FOE	DBE	MCE
SC-MRF	0.94	0.655	1.814	2.623	0.499	1.043	1.487
H40K133A5	0.95	0.547	1.667	2.416	0.506	0.980	1.481
H40K133A15	0.95	0.530	1.529	2.336	0.534	0.932	1.385
H40K167A15	0.93	0.519	1.376	2.170	0.521	0.932	1.362
H40K167A5	0.93	0.621	1.671	2.494	0.520	1.036	1.462
H40K133A10	0.95	0.530	1.510	2.319	0.526	0.918	1.356
H40K167A10	0.93	0.531	1.433	2.264	0.542	0.954	1.316
H40K133A24	0.95	0.530	1.448	2.294	0.519	0.919	1.508
H35K133A5	0.95	0.576	1.788	2.598	0.509	0.911	1.428
H35K133A15	0.95	0.542	1.655	2.353	0.506	0.918	1.341
H35K167A15	0.93	0.501	1.384	2.147	0.489	0.903	1.416
H35K167A5	0.93	0.635	1.745	2.538	0.556	0.966	1.418
H35K133A10	0.95	0.546	1.683	2.379	0.495	0.910	1.392
H35K167A10	0.93	0.500	1.396	2.136	0.494	0.899	1.400
H35K200A10	0.91	0.506	1.534	2.140	0.504	0.887	1.367
H35K133A20	0.95	0.522	1.542	2.299	0.515	0.914	1.364
H30K133A10	0.95	0.543	1.667	2.299	0.470	0.864	1.364

509
510 The maximum values of PFA from all the floors of all the SC-MRF-CBs are lower than that of

511 the SC-MRF under the DBE. Under the FOE and MCE, all the values of PFA of the SC-MRF-

512 CBs are lower than that of the SC-MRF, with the exception of H35K167A5 and H40K133A24

513 for the FOE and MCE, respectively. The PFA reduction observed in the SC-MRF-CBs ranges

514   from 5.81% to 23.65%, from 0.73% to 17.19% and from 0.42% to 11.46%, under the FOE,

515   DBE and MCE, respectively. Thus, the new self-centering column bases can be very effective

516   in reducing the PFA of an SC-MRF that will be equipped with these column bases.

517   These results show that the SC-MRF-CBs have in general better seismic performance than the

518   SC-MRF in terms of the above two engineering demand parameters examined. Low values of

519     $\theta_{s,max}$ and PFA are associated with low non-structural and equipment damage. Thus, non-

520   structural elements and equipment installed to SC-MRF-CBs may exhibit less damage. In

521   addition, since $\theta_{s,max}$ dictates the design of columns in the serviceability limit state, there is a

522   potential of reducing the cross-sections of the members of the SC-MRF-CBs because they

523   exhibit very low values of $\theta_{s,max}$.

524   Figure 5 depicts the comparison of the height-wise distribution of $\theta_{s,max}$, of all the frames

525   studied herein under the FOE, DBE and MCE. Under the FOE, the H40K167A15,

526   H40K167A10, H40K133A24, H35K167A15, H35K167A10 and H35K200A10 have lower

527   values of $\theta_{s,max}$, for all the storeys. The rest of the SC-MRF-CBs have lower values of $\theta_{s,max}$, for

528   all the storeys, with the exception of the first storey. It is also observed that the SC-MRF-CBs

529   have lower values of $\theta_{s,max}$, for all the storeys, with the exception of the first storey under the

530   DBE level. The same trend is observed for all the frames at the MCE level, with the exception

531   of H35K200A10, H35K167A15, H35A167A10 and H40K167A15, which have lower values

532   of $\theta_{s,max}$ for all the storeys. The reason for the increased first-storey $\theta_{s,max}$ demands of most of

533   the SC-MRF-CBs is attributed to the gap openings of their self-centering column bases.

(a)

(b)

(c)

536

537   Figure 6 shows the comparison of the height-wise distribution of PFA under the FOE, DBE

538   and MCE. Under the FOE, apart from the H35K200A10, all the other SC-MRF-CBs have

539   higher PFAs compared to that of the SC-MRF. In the second storey, all the SC-MRF-CBs have

540   higher PFAs compared to that of the SAC-MRF. In the third storey, there is a shift in this trend;

541   H30K133A10, H35K133A10, H40K133A24 and H35K133A15 have lower PFAs than that of

542   the SC-MRF. In the fourth storey, only H35K133A5, H40K133A5, H35K167A5 and

543   H40K167A5 have higher PFAs than that of the SC-MRF. Finally, in the fifth storey, apart from

544   H40K167A5, all the other SC-MRF-CBs have lower PFAs compared to that of the SC-MRF.

545   Under the DBE, the SC-MRF has PFAs lower than those of all the SC-MRF-CBs in both the

546   first and second storey. However, in the third storey, apart from H35K167A4 and H40K176A5

547   which have higher PFAs, and H40K167A10 which has similar PFA, all the other SC-MRF-

548   CBs have lower PFAs compared to that of the SC-MRF. Finally, in both the fourth and fifth

549   storeys, all the SC-MRF-CBs have lower PFAs comparted to that of the SC-MRF. Under the

27

550 MCE, apart from H35K133A15 that has lower PFA in its second storey, all the other SC-MRF-

551 CBs have higher PFAs in all their three first storeys as compared to those of the SC-MRF. In

552 the fourth storey, H40K167A15, H35K167A10 and H35K167A15 have lower PFAs as

553 compared to the SC-MRF. Lastly, in the fifth storey, all the SC-MRF-CBs have lower PFAs

554 compared to that of the SC-MRF.

(a)

(b)

(c)
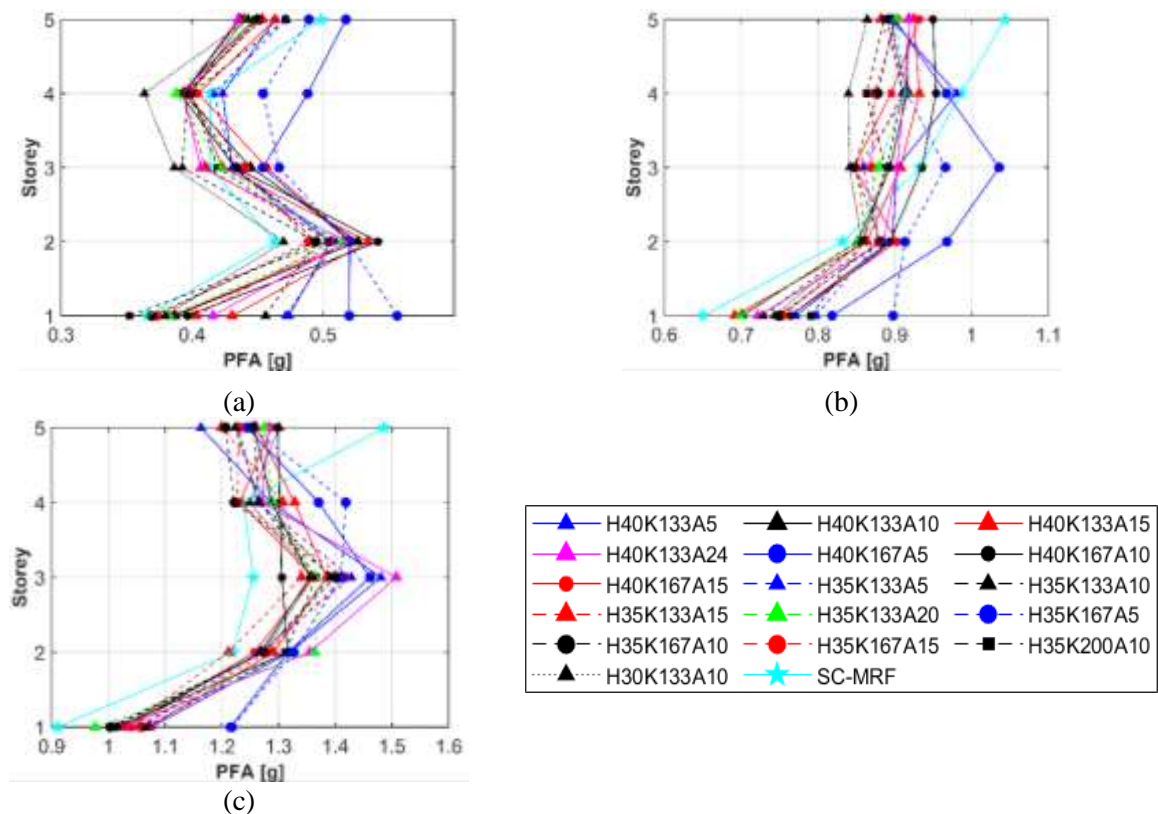
555 Figure 6 Comparison of the median height-wise distribution of the PFA of the SC-MRF and SC-
556 MRF-CBs under the: (a) FOE; (b) DBE; and (c) MCE intensity levels.

557

558 The PFA distribution of Figure 6 can be explained by recent studies in self-centering MRFs

559 with connections similar to those of the SC-MRF-CBs. These suggest that the magnitudes of

560 the PFAs and their distribution is influenced by the interactions between the beams and

561 columns of these systems. These member interactions are due to the discontinuity of their

562 connections and the asymmetry in member restraints due to the presence of the rocking in the

563 column bases [61].

564   *5.2   Effect of base strength and stiffness on the seismic performance of the frames*

565   In this section, the effect of base strength and stiffness on the seismic performance of the frames

566   examined herein is evaluated in terms of $\theta_{s,max}$ and PFA. The parameters η, β_{base} and α, that are

567   associated with the base strength and stiffness of the frames, were used for this evaluation.

568   In order to evaluate the effect of base strength of the frames to the response parameters $\theta_{s,max}$

569   and PFA, the parameter η is examined. Thus, the design cases H40K133A10, H35K133A10

570   and H30K133A10, with η equals 0.40, 0.35 and 0.30, respectively, were compared. Figures

571   7(a) and 7(b) show $\theta_{s,max}$ and PFA versus η, respectively, for the three seismic intensities

572   examined. As indicated in Figure 7(a), when η increases from 0.30 to 0.35, $\theta_{s,max}$ also increases

573   for all the seismic intensity levels. The increase observed is 0.65%, 0.93% and 3.36% under

574   the FOE, DBE and MCE, respectively. A further increase of η to 0.40 results in a reduction of

575    $\theta_{s,max}$ for all the seismic intensity levels. The reduction of $\theta_{s,max}$ is 2.98%, 10.27% and 2.52%

576   under the FOE, DBE and MCE, respectively. The same trend is observed for the PFA but only

577   for the MCE intensity level. Under FOE and DBE, an increase of η results in an increase of

578   PFA. More specifically, when η increases from 0.30 to 0.35, PFA values increase by 5.07%

579   and 5.02%, under the FOE and DBE, respectively. A further increase of η to 0.40 results in an

580   increase of PFA equal to 6% and 0.94%, under the FOE and DBE, respectively.
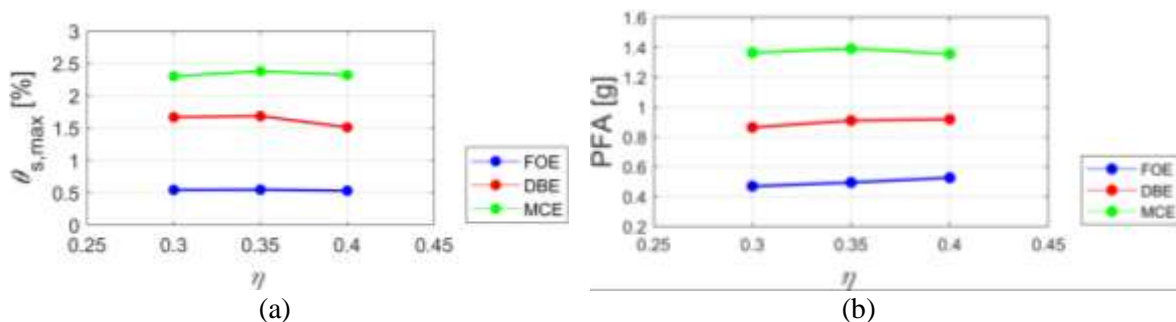
581
582   (a)   (b)
583   Figure 7 Effect of η to (a) $\theta_{s,max}$; and (b) PFA.
584
585   The design cases examined herein were compared in terms of the parameters β_{base} and α to

586   evaluate the effect of base stiffness on their seismic response. For the frames with η=0.40, the

587   following design cases were compared to evaluate the effect of β_{base}, i.e.: H40K133A5

588   (β_{base}=133%) and H40K167A5 (β_{base}=167%), which have a value of α=5%; H40K133A10

589   (β_{base}=133%) and H40K167A10 (β_{base}=167%), with α = 10%; and H40K133A15 (β_{base}=133%)

590   and H40K167A15, with α=15%. For the frames with η=0.35, the following frames were

591   compared: H35K133A5 (β_{base}=133%) and H35K167A5 (β_{base}=167%), with α=5%;

592   H35K133A10 (β_{base}=133%), H35K167A10 (β_{base}=167%) and H35K200A10 (β_{base}=200%),

593   with α=10%; and H35K133A15 (β_{base}=133%) and H35K167A15 β_{base}=167%), with α=15%.

594   Figure 8 shows the effect of β_{base} to the seismic response, in terms of the $\theta_{s,max}$ and PFA, of the

595   aforementioned design cases.

596   For the frames with η=0.40 and α=5%, the results in Table 3 show that an increase of β_{base} from

597   133% to 167% results to higher values of $\theta_{s,max}$, for all the intensity levels. Thus, the increase

598   of $\theta_{s,max}$ observed, due to the increase of β_{base}, is 11.91%, 0.25% and 3.11%, for the FOE, DBE

599   and MCE seismic intensity levels, respectively. The same increase of β_{base}, leads to a reduction

600   of $\theta_{s,max}$ for all the seismic intensity levels for the frames with η=0.40 and α=10%. The

601   reduction observed equals 2.09%, 10.01% and 7.09%, under the FOE, DBE and MCE,

602   respectively. Finally, an increase of β_{base} from 133% to 167% results to lower $\theta_{s,max}$ for the

603   frames with η=0.40 and α=15%, under the DBE and MCE. This trend is reversed under the

604   FOE. In addition, the increase of β_{base} from 133% to 167 results to higher values of PFA under

605   the FOE and DBE, for the frames with η=0.40 and α=5% and α=10%. In contrary, the same

606   increase of β_{base} leads to a reduction of PFA under all the seismic intensity levels for the frames

607   with η=0.40 and α=15%.

608   For the frames with η=0.35 and α=10% and α=15%, results in Table 3 show that an increase of

609   β_{base} from 133% to 167% results to lower values of $\theta_{s,max}$, for all the seismic intensity levels.

610   For the frames with α=10%, the reduction of $\theta_{s,max}$, due to the increase of β_{base}, is 8.46%,

611   17.09% and 10.21%, under the FOE, DBE and MCE, respectively. For the frames with α=10%,

612   this reduction equals 7.56%, 16.40% and 8.76% under the FOE, DBE and MCE. In the frames

613 with $\eta=0.35$ and $\alpha=5\%$, an increase of β_{base} from 133% to 167% results to 2.43% and 2.31%

614 lower values of $\theta_{s,max}$, under the DBE and MCE, respectively. An opposite trend is observed

615 under the FOE. For the frames with $\eta=0.35$ and $\alpha=5\%$, results show that an increase of β_{base}

616 from 133% to 167% results to 8.46% and 5.63% higher values of PFA under the FOE and

617 DBE, respectively. Under the MCE, the PFA of the frame with $\beta_{base}=133\%$ is 0.68% larger

618 than that of with $\beta_{base}=167\%$. For the frames with $\eta=0.35$ and $\alpha=10\%$, results show that an

619 increase of β_{base} from 133% to 167% results to 0.08% and 1.14% lower values of PFA under

620 the FOE and DBE, respectively. Under the MCE, the PFA of the frame with $\beta_{base}=167\%$ is

621 0.56% larger than that of with $\beta_{base}=133\%$. A similar trend is observed for the frames with

622 $\eta=0.35$ and $\alpha=15\%$.

(a)   (b)

(c)   (d)
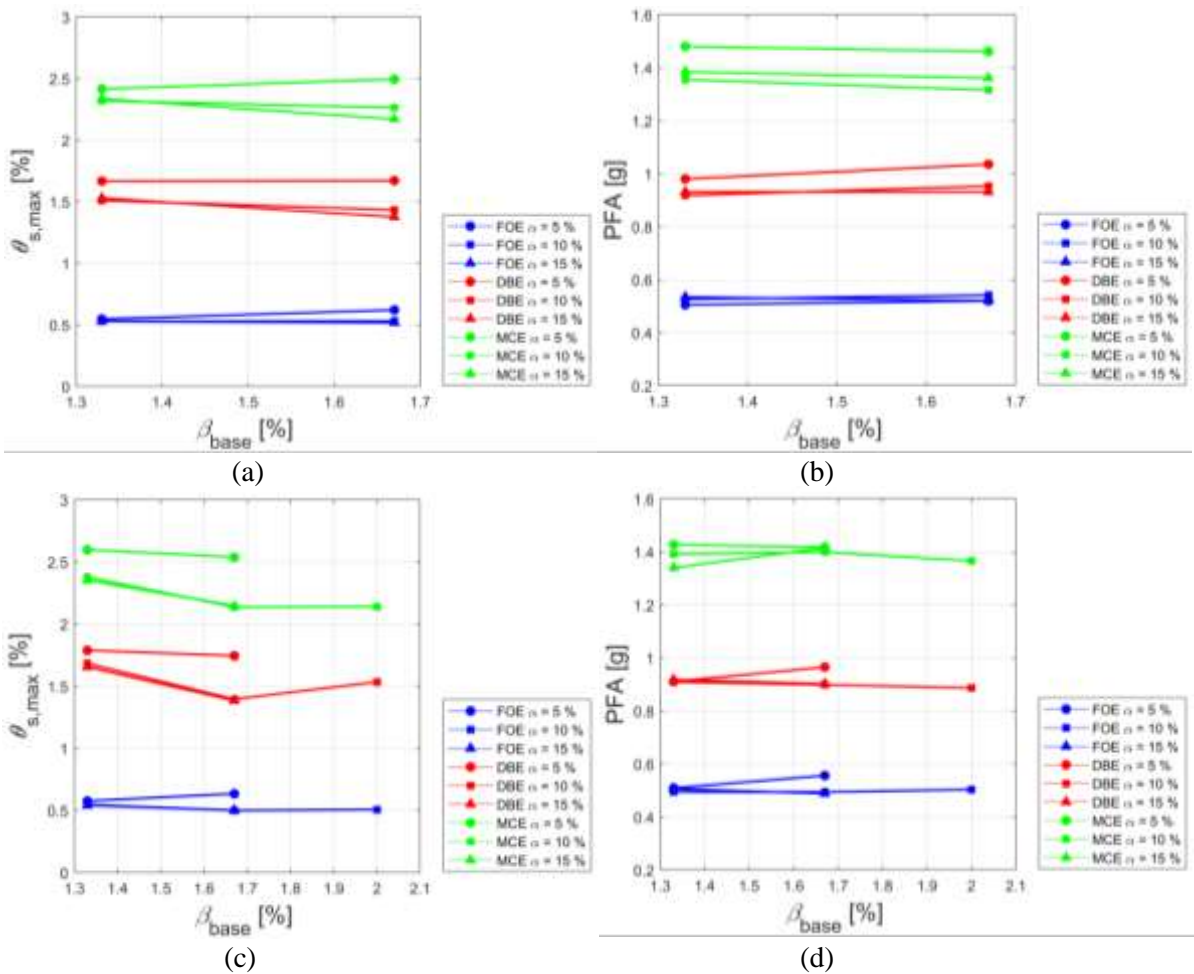
Figure 8 Effect of β_{base} to (a) $\theta_{s,max}$ ($\eta = 0.40$); (b) PFA ($\eta = 0.40$); (c) $\theta_{s,max}$ ($\eta = 0.35$); and (d) (b) PFA ($\eta = 0.35$).

630   For the design cases with η=0.40, the following frames were compared to evaluate the effect

631   of α on $\theta_{s,max}$ and PFA: H40K133A5 (α=5%), H40K133A10 (α=10%), H40K133A15 (α=15%)

632   and H40K133A24 (α=24.5%), with β_{base}=133%; and H40K167A5 (α=5%), H40K167A10

633   (α=10%) and H40K167A15 (α=15%), with β_{base}=167%. This effect is shown in Figures 9(a)-

634   (d) for these design cases. It is observed that the highest value of $\theta_{s,max}$ is achieved by

635   H40K133A5 (α=5%) for the frames with β_{base}=133%, under the FOE, DBE and MCE. The

636   lowest values of $\theta_{s,max}$ are achieved for the frame H40K133A24 (α=24.5%) for both the DBE

637   and MCE. Frame H40K133A5 with α=5% has the best PFA performance, achieving the lowest

638   value of PFA under the FOE. In addition, the frame with α=10% has the best PFA performance

639   under the DBE and MCE. For the frames with β_{base}=167%, increasing the value of α from 5%

640   to 10%, results in a reduction of $\theta_{s,max}$ for all the seismic intensity levels. This reduction equals

641   14.48%, 14.22% and 9.21%, under the FOE, DBE and MCE, respectively. A further increase

642   of α from 10% to 15%, leads to a reduction of $\theta_{s,max}$, which equals 2.31%, 3.98% and 4.23%,

643   under the FOE, DBE and MCE, respectively. Increasing the value of α from 5% to 10%, leads

644   to a 3.95% increase, and 7.94% and 9.93% reduction of PFA under the FOE, DBE and MCE,

645   respectively. Finally, a further increase of α from 10% to 15%, leads to a 3.76% and 2.29%

646   reduction and 3.32% increase of PFA, under the FOE, DBE and MCE, respectively.

647   For the design cases with η=0.35, the following frames were compared: H35K133A5 (α=5%),

648   H35K133A10 (α=10%), H35K133A15 (α=15%) and H35K133A20 (α=20%), with

649   β_{base}=133%; and H35K167A5 (α=5%), H35K167A10 (α=10%) and H35K167A15 (α=15%),

650   with β_{base}=167% (Figures 9(e)-(h)). For the frames with β_{base}=133%, the lowest values of $\theta_{s,max}$

651   is achieved for the frame with the higher value of α, i.e., 20% (H35K133A20), for all the

652   seismic intensity levels. The frame with α=5% (H35K133A10) has the best PFA performance,

653   achieving the lowest value of PFA under DBA and MCE. In addition, the frame α=15% has

654   the best PFA performance under the MCE. For the frames with β_{base}=167%, increasing the

655   value of α from 5% to 10%, results in a reduction of $\theta_{s,max}$ for all the seismic intensity levels.

656   This reduction equals 21.26%, 20.02% and 15.83%, under the FOE, DBE and MCE,

657   respectively. A further increase of α from 10% to 15%, leads to a 0.23% increase, 0.83%

658   reduction and 0.49% increase of $\theta_{s,max}$, under the FOE, DBE and MCE, respectively. Increasing

659   the value of α from 5% to 10%, leads to a 11.14%, 6.89% and 1.30% reduction of PFA under

660   the FOE, DBE and MCE, respectively. Finally, a further increase of α from 10% to 15%, results

661   to a 1.14% reduction, and 0.38% and 1.14% increase of PFA, under the FOE, DBE and MCE,

662   respectively.
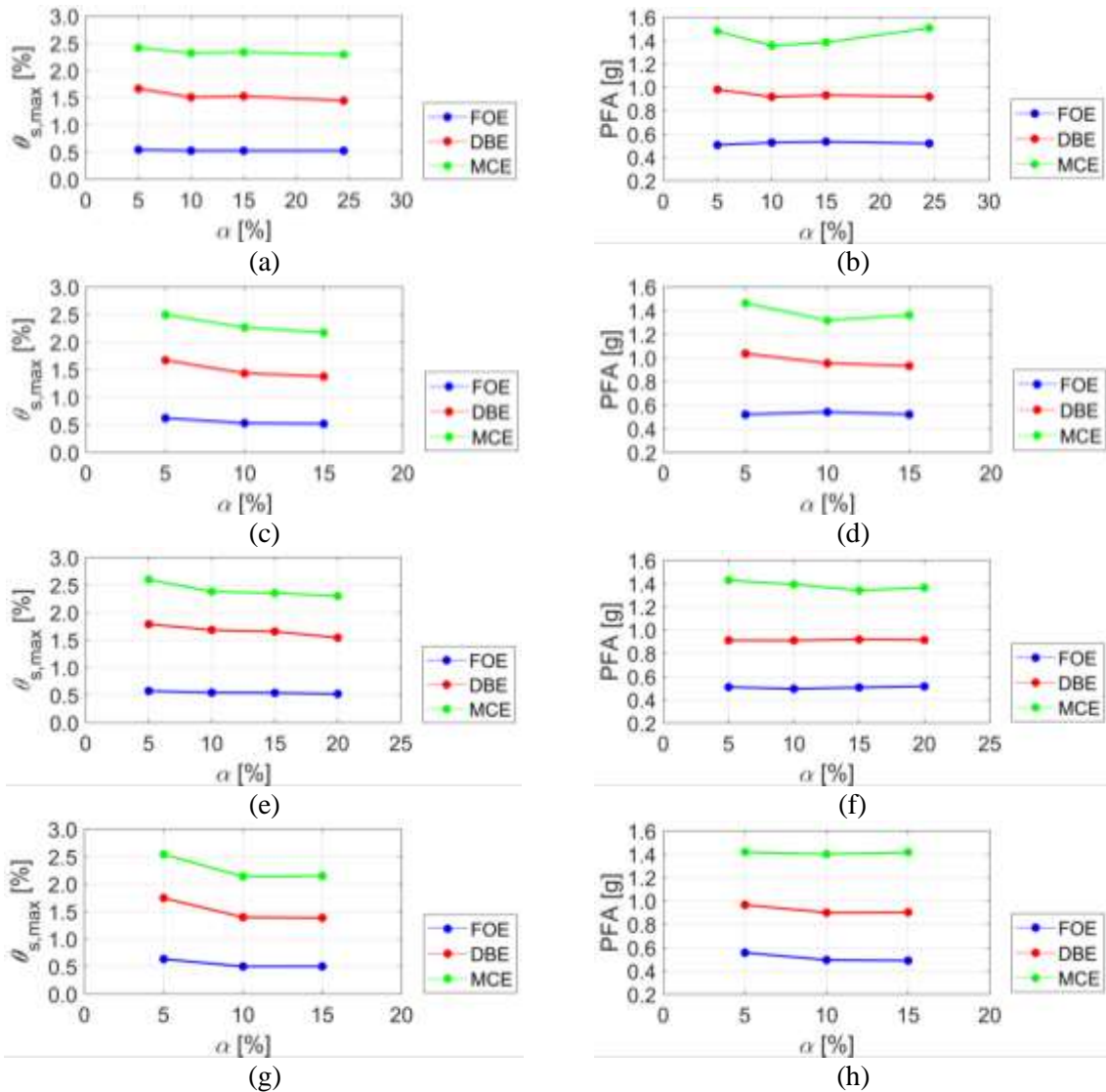
663   Figure 9 Effect of α to (a) $\theta_{s,max}$ ($\eta = 0.40$, $\beta_{base} = 133\%$); (b) PFA ($\eta = 0.40$, $\beta_{base} = 133\%$); (c) $\theta_{s,max}$ (η
664    $= 0.40$, $\beta_{base} = 167\%$); (d) PFA ($\eta = 0.40$, $\beta_{base} = 167\%$); (e) $\theta_{s,max}$ ($\eta = 0.35$, $\beta_{base} = 133\%$); (f) PFA (η
665    $= 0.35$, $\beta_{base} = 133\%$); (g) $\theta_{s,max}$ ($\eta = 0.35$, $\beta_{base} = 167\%$); and (h) PFA ($\eta = 0.35$, $\beta_{base} = 167\%$).

666

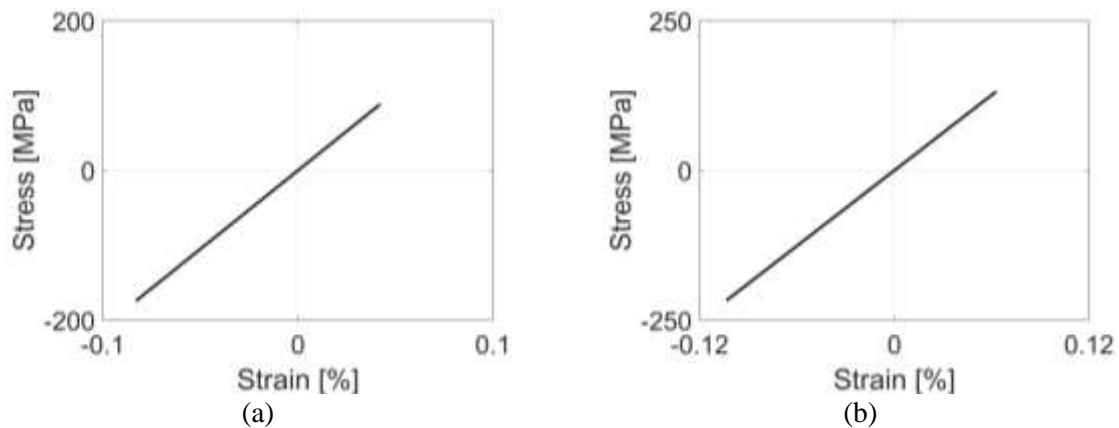667   *5.3   Residual drift performance of the frames*

668   Figure 10 shows the height-wise distribution of the median residual drifts ($\theta_{s,res}$) of the SC-

669   MRF, H35K133A5 and H35K200A10 under the MCE, together with a maximum allowable

670   limit for residual drifts. This limit was proposed by McCormick et al. [62] and utilised to

671   characterise repairability in such buildings. The rationale for presenting only these two SC-

672   MRF-CBs is that they are those that exhibit the lowest and highest $\theta_{s,res}$ values among the

673   investigated frames. Residual drifts are recognised as an important index of the seismic

674   performance and resilience of structures since they are directly linked to probability of

675   demolition of a building [34,62]. It is observed that all the frames have values of $\theta_{s,res}$ lower

676   than the proposed limit in [62] and that both H35K133A5 and H35K200A10 have lower $\theta_{s,res}$

677   values for all their storeys than those of the SC-MRF. These values are almost negligible.
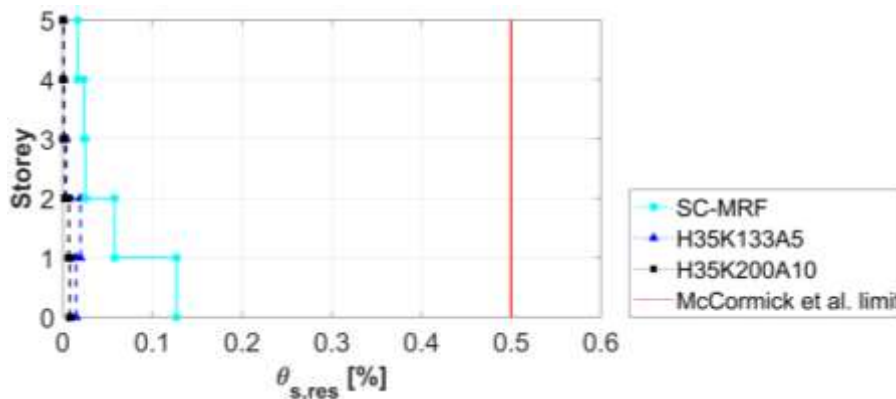
678   Figure 10 Height-wise distribution of median residual drifts of the SC-MRF, H35K133A5 and
679   H35K200A10 under the MCE, plotted against the maximum allowable limit for residual interstorey
680   drifts proposed by McCormick et al. [62].

682   Figure 11 shows the stress-strain hysteresis loops in the flanges of the first-storey columns

683   (Figure 3(a)) of the H35K133A5 and H35K200A10 under the 1992 Landers earthquake scaled

684   to the MCE. It is observed, that the two SC-MRF-CBs do not exhibit any plastic deformation

685   in their first-storey columns since the developed maximum stress at the extreme fibers of their

686   flanges is well below the yield stress limit of 355 MPa. Thus, damage is avoided at their self-

687   centering column bases. This shows that the values of $\theta_{s,res}$ observed in SC-MRF-CBs (Figure

688   10) mainly result from permanent deformations that occur at PT beam-column connections.

34

689 Similar results are observed for the rest of the SC-MRF-CBs and ground motions but are not

690 shown herein due to lack of space.

693
694 **6   COLLAPSE ASSESSMENT**

695 The collapse resistance of the frames is determined by the use of IDA [63]. $S_a(T_1)$ is the IM

696 used herein and $\theta_{s,max}$ was the response parameter monitored. The set of ground motions used

697 for the non-linear dynamic analyses in Section 5 were used also for the IDAs. For each design

698 case and ground motion, the collapse $S_a(T_1)$ value at which $\theta_{s,max}$ increases without bound was

699 obtained. To determine the limit of collapse, the criterion adopted by Seo et al. [64] was used.

700 Thus, the incremental slopes were calculated by drawing straight lines between the consecutive

701 data points in the IDA curve. The lowest $S_a(T_1)$ value corresponding to the ith data point with

702 the slope between the ith and $i+1^{th}$ points being less than 10% of the initial slope on the IDA

703 curve was defined as the collapse $S_a(T_1)$. The initial slope was determined from the straight line

704 from the origin of axis to the first data point of the IDA curve. A collapse fragility curve was

705 generated by fitting a lognormal cumulative distribution function to the collapse $S_a(T_1)$ values

706 determined for each frame. The median value, S_{CT}, and the lognormal standard deviation, β, of

707 collapse $S_a(T_1)$ values define this distribution. The value of S_{CT} was amplified to take into

708 account the effect of the distinct spectral shape of rare ground motions, characterised by the

709 parameter ε [65]. In this work, the simplified methodology proposed by FEMA P695 [59] is

710   adopted, where the influence of the spectral shape is taken into account by the use of a spectral

711   shape factor (*SSF*). Thus, the values of S_{CT} of all the frames of this study were multiplied by

712   *SSF* to estimate their true collapse capacity.

713   The parameter *β* affects the shape of the fragility curve and is a measure of the level of

714   uncertainty in the analysis results. The system-level and the record-to-record uncertainty were

715   used for the construction of the fragility curves. The FEMA P695 [59] regulations were used

716   for the calculation of the total uncertainty, where additional system-level uncertainty were

717   added from three categories [43]. The total uncertainty of the system, β_{Total}, is given by:

718    $$\beta_{Total} = \sqrt{\beta_{RTR}^2 + \beta_{DR}^2 + \beta_{TD}^2 + \beta_{MDL}^2}$$ (13)

719   where β_{RTR} is the record-to-record uncertainty, β_{DR}, β_{TD} and β_{MDL} are the additional uncertainty

720   because of the robustness of the design requirements, the accuracy of the test data and the

721   accuracy of the numerical model, respectively. The values of β_{RTR} were taken from the results

722   of the IDA, while values of the rest uncertainties were based on P695 recommendations [59].

723   Thus, the uncertainties β_{DR}, β_{TD} and β_{MDL} can be subjectively classified as 'superior', 'good',

724   'fair', or 'poor' [59]. The uncertainty due to the robustness of the design requirements, accuracy

725   of the test data and numerical model were assigned each rating of 'superior', 'good', 'fair' and

726   'poor' together to construct four different collapse fragility curves. The values of uncertainty

727   for 'superior', 'good', 'fair' and 'poor' uncertainty rating were 0.1, 0.2, 0.35 and 0.5,

728   respectively. Figure 12 shows the IDA curves of the H35K200A10 together with the collapse

729   fragility curves, for different uncertainty ratings as per the aforementioned procedure.

(a)

(b)
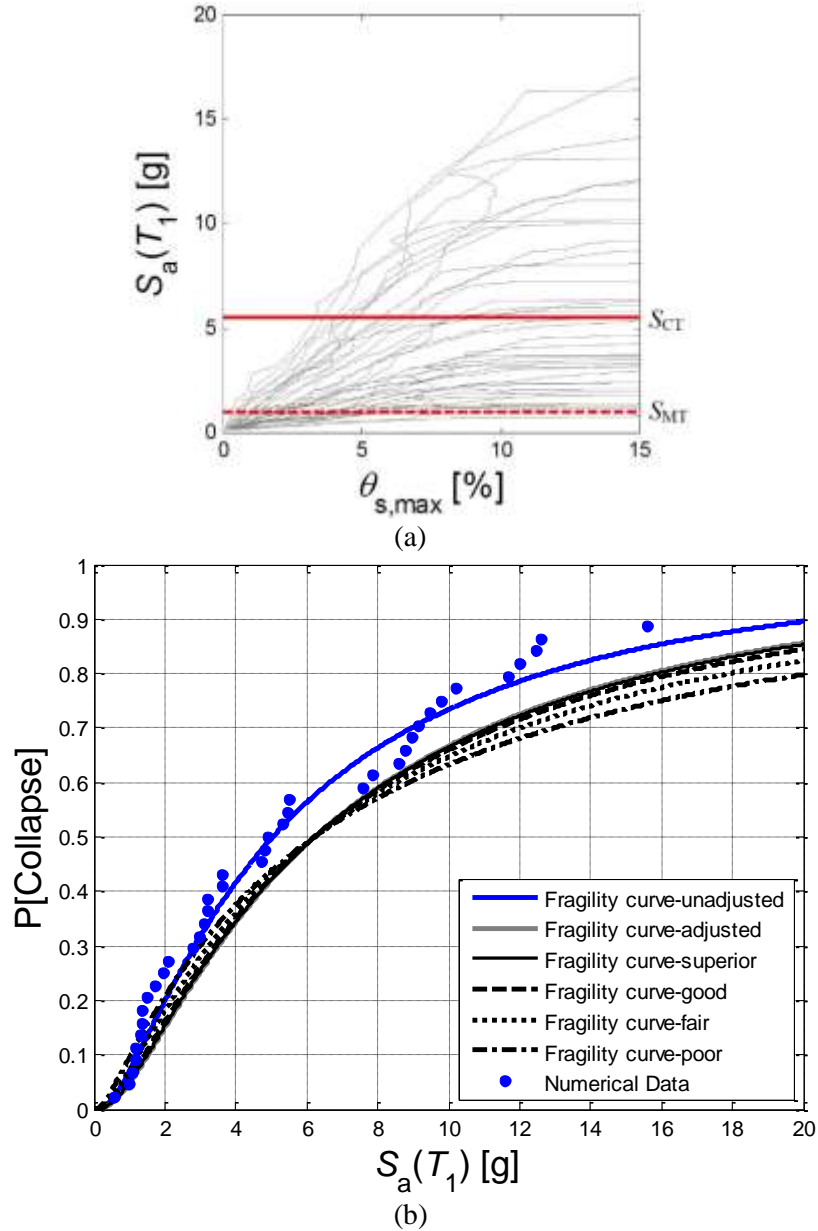
Figure 12 (a) IDA curves; and (b) corresponding collapse fragility curves of the H35K200A10.

Finally, the constructed collapse fragility curves were used for the evaluation of the collapse

risk of the frames through the adjusted collapse margin ratio (*ACMR*), defined as:

$$ACMR = \frac{S_{CT}}{S_{MT}} \cdot SSF \tag{14}$$

where S_{CT}, is the median collapse intensity of the frames, S_{MT} is intensity demand to the MCE-

level intensity and *SSF* is the spectral shape factor.

737 **7   EFFECT OF BASE STRENGTH AND STIFFNESS ON THE COLLAPSE RISK OF**
738 **THE FRAMES**

739 Table 4 shows the collapse capacity results of all the investigated frames. The SC-MRF-CBs

740 have larger value of collapse capacity and *ACMR*, compared to the SC-MRF. The maximum

741 increase in collapse capacity and *ACMR* is achieved by the H35K200A10 compared to SC-

742 MRF, whereas the minimum increase of these parameters is achieved by the H35K133A5.

743 Collapse capacity and *ACMR* of the SC-MRF-CBs design cases are 25.08-33.23% and 23.02-

744 27.95% higher, respectively, than that of the SC-MRF. Thus, there is a significant improvement

745 of the collapse capacity and *ACMR*, by adopting the self-centering column bases and

746 appropriately tuning their base stiffness and strength characteristics.

747 Figure 13 shows the collapse fragility curves of the SC-MRF, H35K133A5 and H35K200A10

748 for different uncertainty ratings. These two SC-MRF-CBs were selected because they achieve

749 the lower and higher increase of *ACMR*, compared to the SC-MRF. It is observed that the

750 H35K133A5 and H35K200A10 are exhibiting, in general, the lowest probabilities of collapse.

751 This trend is inverted for low values of $S_a(T_1)$, for superior, good and fair uncertainty ratings,

752 and for poor uncertainty ratings the probabilities of collapse are similar for all the frames.

753

Table 4. Collapse capacity results.

Frame	S_{MT} (g)	S_{CT} (g)	*CMR*	*SSF*	*ACMR*
SC-MRF	0.90	3.70	4.10	1.23	5.06
H40K133A5	0.93	5.04	5.44	1.23	6.72
H40K133A15	0.93	5.17	5.57	1.23	6.88
H40K167A15	0.95	5.39	5.67	1.23	6.97
H40K167A5	0.95	5.28	5.56	1.23	6.83
H40K133A10	0.93	5.19	5.60	1.23	6.92
H40K167A10	0.95	5.38	5.66	1.23	6.95
H40K133A24	0.92	5.04	5.45	1.24	6.74
H35K133A5	0.93	4.94	5.32	1.23	6.57
H35K133A15	0.93	5.18	5.59	1.23	6.87
H35K167A15	0.95	5.32	5.60	1.23	6.89
H35K167A5	0.95	5.27	5.54	1.23	6.80
H35K133A10	0.93	5.19	5.60	1.23	6.91
H35K167A10	0.95	5.35	5.64	1.23	6.92

H35K200A10	0.97	5.54	5.74	1.22	7.02
H35K133A20	0.93	5.04	5.43	1.23	6.70
H30K133A10	0.93	5.11	5.51	1.23	6.81

754

755 To evaluate the effect of base strength on the collapse risk of the frames, the base strength

756 factor η was utilised. To this end, the design cases H40K133A10, H35K133A10 and

757 H30K133A10, with η equals 0.40, 0.35 and 0.30, respectively, were compared. The

758 H40K133A10 has the largest value of *ACMR* among the frames compared, indicating that the

759 frame with the largest value of η has the lowest collapse risk. When the value of η is increased

760 from 0.30 to 0.35, the *ACMR* is increased by 1.5%. In addition, the value of *ACMR* for the

761 H40K133A10 with $\eta = 0.40$ is 1.61% higher than that of the H30K133A10 with $\eta = 0.30$. Thus,

762 the collapse risk of the frames is reduced for higher values of η.

763 The frames examined here were compared in terms of their base factors β_{base} and α to assess

764 the effect of base stiffness on their collapse risk. For the frames with η=0.40, the following

765 frames were compared to evaluate the effect of β_{base}, i.e.: H40K133A5 (β_{base}=133%) and

766 H40K167A5 (β_{base}=167%), which have a value of α=5%; H40K133A10 (β_{base}=133%) and

767 H40K167A10 (β_{base}=167%), with α=10%; and H40K133A15 (β_{base}=133%) and H40K167A15,

768 with α=15%. For the frames with η=0.35, the following frames were compared: H35K133A5

769 (β_{base}=133%) and H35K167A5 (β_{base}=167%), with α=5%; H35K133A10 (β_{base}=133%),

770 H35K167A10 (β_{base}=167%) and H35K200A10 (β_{base}=200%), with α=10%; and H35K133A15

771 (β_{base}=133%) and H35K167A15 (β_{base}=167%), with α=15%.

772 The results in Table 4 indicate that an increase of β_{base} from 133% to 167% results to higher

773 values of *ACMR* for the frames with η=0.40. Thus, the increase of *ACMR* observed, due to the

774 increase of β_{base}, is 1.63%, 0.46% and 1.21% for the design cases with α equals 5%, 10% and

775 15%, respectively. Similar results are obtained for the frames with η=0.35. The values of

776 *ACMR* of the frames with β_{base} equal to 167% are 3.40%, 0.12% and 0.29% higher than those

777 of the frames with β_{base} equal to 133%, when α equals 5%, 10% and 15%, respectively. In

778 addition, the frame H35K200A10 (β_{base}=200%) has 1.46% and 1.58% higher values of *ACMR*

779 than those of the H35K167A10 (β_{base}=167%) and H35K133A10 (β_{base}=133%), respectively.

780 Thus, it can be concluded that the collapse resistance of the frames is increased for frames with

781 higher values of β_{base}, representing the initial base stiffness.

782
783
(a)   (b)
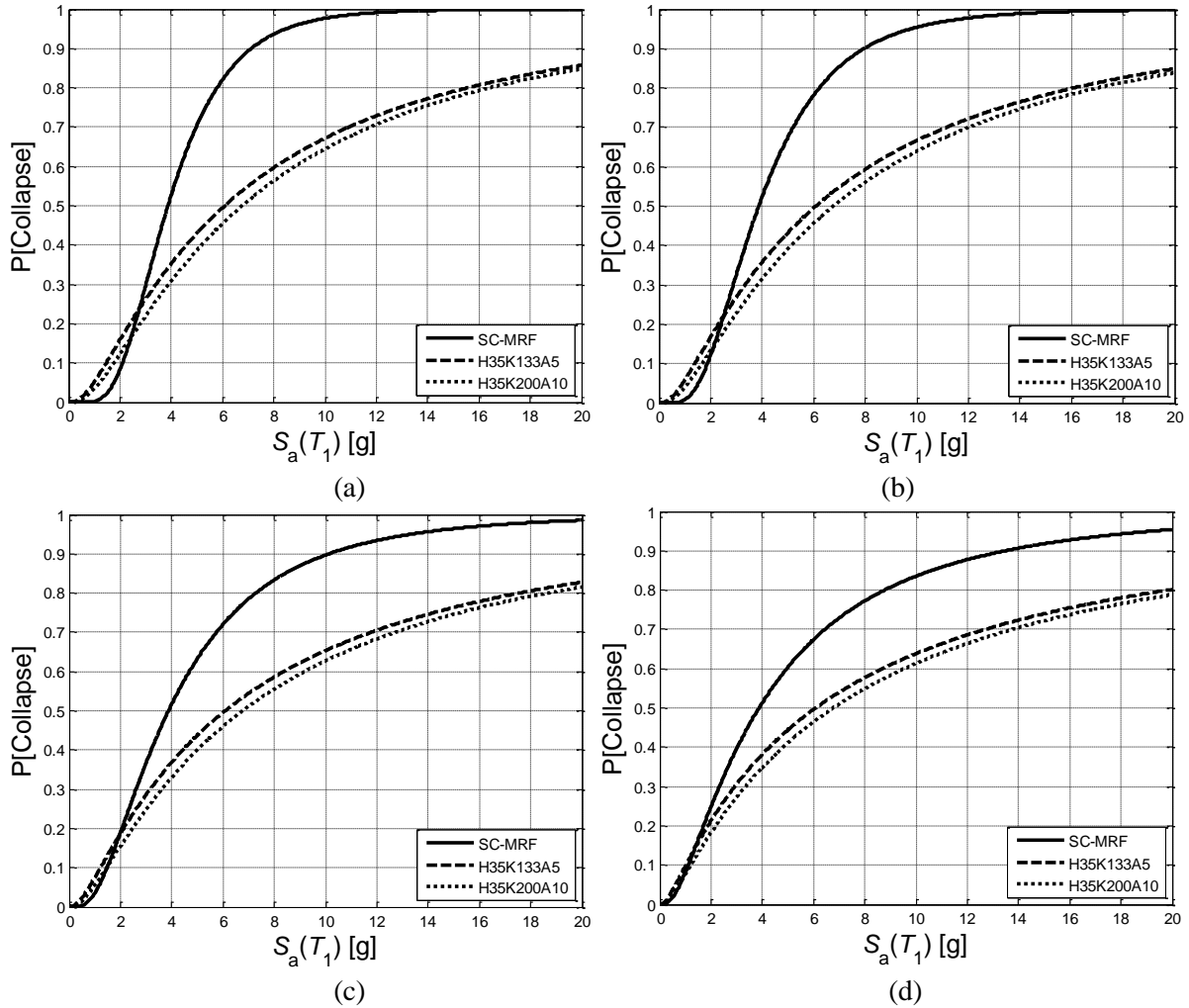
784
785 (c)   (d)
786 Figure 13 Collapse fragility curves of SC-MRF, H35K133A5 and H35K200A10 for: (a) superior; (b)
787 good; (c) fair; and (d) poor uncertainty rating.

788
789 For the design cases with η=0.40, the following frames were compared to evaluate the effect

790 of α: H40K133A5 (α=5%), H40K133A10 (α=10%), H40K133A15 (α=15%) and

791 H40K133A24 (α=24.5%), with β_{base}=133%; and H40K167A5 (α=5%), H40K167A10

792 (α=10%) and H40K167A15 (α=15%), with β_{base}=167%. The results indicate that the higher

793 value of *ACMR* is achieved by H40K133A10 (α=10%), for the frames with β_{base}=133%. Thus,

794 collapse resistance of the frames is increased by 2.89% when α increases from 5% to 10%, and

795 is then reduced for further increase of α. For the frames with β_{base}=167% a different trend is

796 observed, with *ACMR* having higher values when α increases. Thus, the frame H40K167A15

797 (α=15%) has 0.22% and 1.96% higher values of *ACMR* than those of H40K167A10 (α=10%)

798 and H40K167A5 (α=5%), respectively.

799 For the design cases with η=0.35 the following frames were compared: H35K133A5 (α=5%),

800 H35K133A10 (α=10%), H35K133A15 (α=15%), and H35K133A20 (α=20%), with

801 β_{base}=133%; and H35K167A5 (α=5%), H35K167A10 (α=10%) and H35K167A15 (α=15%),

802 with β_{base}=167%. The results of the frames with β_{base}=133% demonstrate that the *ACMR* is

803 increased when α is increased from 5% to 15% and is then reduced for further increase of α. A

804 similar trend is observed for the frames with β_{base}=167%.

8 CONCLUSIONS

806 The potential of the SC-MRF-CBs to improve the seismic performance and reduce the collapse

807 risk of earthquake-resilient steel buildings with SC-MRFs was examined. The effect of strength

808 and stiffness characteristics of the novel self-centering column base to improve the seismic

809 performance and collapse capacity of the SC-MRF-CBs was also investigated. The parameters

810 through which these effects were taken into consideration were three normalised factors that

811 represent the initial stiffness, post-yield stiffness and strength of the self-centering column

812 bases. These structural properties of the self-centering column bases can be independently

813 adjusted by utilising the analytical expressions that are presented in this research, thereby

814 changing also the initial stiffness, post-yield stiffness and strength of the whole SC-MRF-CBs.

815 The evaluation of the seismic performance and collapse risk of the SC-MRF-CBs was based

816 on a prototype steel building designed to incorporate different seismic-resistant frames, i.e.,

817 one SC-MRF and sixteen SC-MRF-CBs' designs with different base stiffness and strength

818 characteristics. A set of 44 ground motions that were scaled to three seismic intensity levels

819 was utilised to perform non-linear dynamic analyses and evaluate the seismic performance of

820   the frames. Moreover, IDA was used with the same set of ground motions to evaluate the

821   collapse capacity of the frames. Finally, fragility curves and the *ACMR* of the frames were

822   derived to compare their seismic risk.

823   On the basis of the findings of this paper, the following conclusions can be drawn:

824   1.   The SC-MRF-CBs have in general better seismic performance than the SC-MRF in

825   terms of $\theta_{s,max}$ and PFA. The results demonstrate that the self-centering column base is

826   very effective in reducing $\theta_{s,max}$ and PFA, by only tuning its base stiffness and strength

827   characteristics. Thus, non-structural elements and equipment installed to SC-MRF-CBs

828   will potentially exhibit less damage. A potential of reducing the cross-sections of the

829   members of the SC-MRF-CBs can be also concluded. That is because the SC-MRF-

830   CBs exhibit $\theta_{s,max}$ values lower than the relevant limits of EC8 under the FOE, DBE

831   and MCE. This reduction reaches an appreciable 24.05%.

832   2.   The H35K133A5 and H35K200A10 (i.e., the two frames that exhibit the lowest and

833   highest values of $\theta_{s,res}$ among the investigated SC-MRF-CBs) have lower values of $\theta_{s,res}$

834   in all their storeys, compared to those of the SC-MRF. These values are almost

835   negligible. In addition, even these values of $\theta_{s,res}$ mainly result from the PT beam-

836   column connections and not from the self-centering column bases since the latter

837   behave elastically and do not exhibit any permanent deformation.

838   3.   The SC-MRF-CBs have superior collapse capacity compared to the SC-MRF. The

839   collapse capacity and *ACMR* of the SC-MRF-CBs are increased by up to 33.23% and

840   27.95%, respectively, compared to the SC-MRF.

841   4.   The collapse risk of the SC-MRF-CBs is reduced for higher values of η. The

842   H40K133A10 with η=0.40 has the largest value of *ACMR* among the frames compared,

843   indicating that the frame with the largest value of η has the lowest collapse risk.

844   5.   It is concluded that collapse capacity of the frames is increased for frames with higher

845   values of β_{base}. The SC-MRF-CBs with β_{base}=167% have superior collapse resistance

846   than the ones with β_{base}=133%, when η=0.40. The maximum increase of *ACMR*

847   observed, due to the increase of β_{base}, is 1.63% for the design cases with α=5%. Similar

848   results are obtained for the frames with η=0.35. The values of *ACMR* of the frames with

849   β_{base}=167% are 3.40%, 0.12% and 0.29% higher than those of the frames with

850   β_{base}=133%, when α equals 5%, 10% and 15%, respectively. In addition, the frame

851   H35K200A10 (β_{base}=200%) has 1.46% and 1.58% higher values of *ACMR* than those

852   of the H35K167A10 (β_{base}=167%) and H35K133A10 (β_{base}=133%), respectively.

853   6.   The results for the SC-MRF-CBs with η=0.40 indicate that the higher value of *ACMR*

854   is achieved by the frame with α=10%, for the frames with β_{base}=133%. Thus, the

855   collapse capacity of the frames increses by 2.89% when α increses from 5% to 10% and

856   is then reduced for further increase of α. For the frames with β_{base}=167%, a different

857   trend is observed, with *ACMR* having higher values when α is increased up to 15%.

858   7.   For the SC-MRF-CBs with η=0.35 and β_{base}=133%, it is observed that the *ACMR* is

859   increased when α is increased from 5% to 15% and is then reduced for further increase

860   of α. A similar trend is observed for the frames with β_{base}=167%.

861   8.   It is concluded that the best seismic performance and highest collapse capacity among

862   the SC-MRF-CBs examined is achieved for a combination of the strength factor, η,

863   equal to 0.35; initial stiffness factor, β_{base}, equal to 200%; and post-yield stiffness ratio,

864   α, equal to 10%.

865 **REFERENCES**

866 [1]   H. Inamasu, D.G. Lignos, A.M. Kanvinde, Effect of column base flexibility on the
867   hysteretic response of wide flange steel columns, 3rd Huixian Int. Forum Earthq. Eng.
868   Young   Res.   August   11-12.   (2017)   Paper   No.   260.
869   https://infoscience.epfl.ch/record/230104/files/260_Inamasu_Hiroyuki_fullpaper.pdf.
870 [2]   F. Zareian, A. Kanvinde, Effect of column-base flexibility on the seismic response and
871   safety of steel moment-resisting frames, Earthq. Spectra. 29 (2013) 1537–1559.

872   doi:10.1193/030512EQS062M.

873 [3]   J. Ruiz-García, A. Kanvinde, Effect of column base flexibility on residual drift demands
874   of low-rise steel moment-resisting frames, in: 2013 World Congr. Adv. Struct. Eng. Eng.
875   Mech. (ASEM13), Sept. 8-12, Jeju, Korea, 2013: pp. 627–639.

876 [4]   P.A. Torres-Rodas, F. Flores, F. Zareian, Seismic Response Of Steel Moment Frame
877   Considering Gravity System And Column Base Flexibility, in: Proc. 11th US Natl. Conf.
878   Earthq.   Eng.,   June   25-29,   Los   Angeles,   USA,   2018.
879   https://www.researchgate.net/profile/Pablo_Torres-
880   Rodas/publication/327663389_Seismic_Response_of_Steel_Moment_Frames_conside
881   ring_gravity_system_and_column_base_flexibility/links/5b9c618292851ca9ed0aa655/
882   Seismic-Response-of-Steel-Moment-Frames-considering.

883 [5]   A. Aviram, B. Stojadinovic, A. Der Kiureghian, Performance and reliability of exposed
884   column base plate connections for steel moment-resisting frames, Berkeley, CA, USA,
885   2010.

886 [6]   BS EN 1998-1, Eurocode 8: Design of structures for earthquake resistance - Part 1:
887   General rules, seismic actions and rules for buildings., 2013.

888 [7]   P.T. Rodas, F. Zareian, A. Kanvinde, Hysteretic Model for Exposed Column–Base
889   Connections, J. Struct. Eng. (2016) 04016137. doi:10.1061/(ASCE)ST.1943-
890   541X.0001602.

891 [8]   D.G. Lignos, H. Krawinkler, A database in support of modeling of component
892   deterioration for collapse prediction of steel frame structures, in: John W. Wallace (Ed.),
893   Struct. Eng. Res. Front. May 16-19, Long Beach, California, United States, 2007: pp.
894   1–12. doi:doi: 10.1061/40944(249)31.

895 [9]   H.-J. Kim, C. Christopoulos, Seismic design procedure and seismic response of post-
896   tensioned self-centering steel frames, Earhtquake Eng. Struct. Dyn. 38 (2009) 355–376.
897   doi:10.1002/eqe.859.

898 [10]   A.S. Tzimas, A.I. Dimopoulos, T.L. Karavasilis, EC8-based seismic design and
899   assessment of self-centering steel frames with viscous dampers, J. Constr. Steel Res. 105
900   (2015) 60–73.

901 [11]   J.M. Ricles, R. Sause, M.E.M. Garlock, C. Zhao, Posttensioned seismic-resistant
902   connections for steel frames, J. Struct. Eng. 127 (2001) 113–121.

903 [12]   K.-C. Tsai, C.-C. Chou, C.-L. Lin, P.-C. Chen, S.-J. Jhang, Seismic self-centering steel
904   beam-to-column moment connections using bolted friction devices, Earthq. Eng. Struct.
905   Dyn. 37 (2008) 627–645. doi:10.1002/eqe.779.

906 [13]   G. Vasdravellis, T.L. Karavasilis, B. Uy, Large-scale experimental validation of steel
907   post-tensioned connections with web hourglass pins, J. Struct. Eng. 139 (2013) 1033–
908   42. doi:10.1061/(ASCE)ST.1943-541X.0000696.

909 [14]   G. Vasdravellis, T.L. Karavasilis, B. Uy, Design rules, experimental evaluation, and
910   fracture models for high-strength and stainless-steel hourglass shape energy dissipation
911   devices, J. Struct. Eng. 140 (2014) 04014087. doi:10.1061/(ASCE)ST.1943-
912   541X.0001014.

913 [15]   P. Rojas, J.M. Ricles, R. Sause, Seismic Performance of Post-tensioned Steel Moment
914   Resisting Frames with Friction Devices, J. Struct. Eng. 131 (2005) 529–540.
915   doi:10.1061/(ASCE)0733-9445(2005)131:4(529).

916 [16]   C.-C. Chou, Y.-C. Wang, J.-H. Chen, Seismic design and behavior of post-tensioned
917   steel connections including effects of a composite slab, Eng. Struct. 30 (2008) 3014–
918   3023. doi:10.1016/j.engstruct.2008.04.013.

919 [17]   M.A. Chowdhury, A. Rahmzadeh, M.S. Alam, Improving the seismic performance of
920   post-tensioned self-centering connections using SMA angles or end plates with SMA
921   bolts, Smart Mater. Struct. 28 (2019) 075044.

922 [18] M.A. Chowdhury, A. Rahmzadeh, S. Moradi, M.S. Alam, Feasibility of using reduced
923   length superelastic shape memory alloy strands in post-tensioned steel beam–column
924   connections, J. Intell. Mater. Syst. Struct. 30 (2018) 283–307.
925   doi:10.1177/1045389X18806393.
926 [19] B. Uy, Innovative connections for the demountability and rehabilitation of steel, space
927   and composite structures, in: 12th Int. Conf. Steel, Sp. Compos. Struct. 28-30 May,
928   Prague, Czech Republic, 2014: pp. 99–109.
929 [20] J. Liu, Design for Deconstruction with Demountable Composite Beams and Floor
930   Systems, Eng. J. 53 (2016) 107–16.
931 [21] S. Pampanin, C. Christopoulos, M.J.N. Priestley, Performance-based seismic response
932   of frame structures including residual deformations. Part II: Multi-degree of freedom
933   systems., J. Earthq. Eng. 7 (2003) 119–147.
934 [22] C. Christopoulos, A. Filiatrault, B. Folz, Seismic response of self-centring hysteretic
935   SDOF systems, Earthq. Eng. Struct. Dyn. 31 (2002) 1131–1150. doi:10.1002/eqe.152.
936 [23] C. Christopoulos, Frequency Response of Flag-Shaped Single Degree-of-Freedom
937   Hysteretic Systems, J. Eng. Mech. 130 (2004) 894–903. doi:10.1061/(ASCE)0733-
938   9399(2004)130:8(894).
939 [24] C. Christopoulos, S. Pampanin, M.J.N. Priestley, Performance-based seismic response
940   of frame structures including residual deformations. Part 1: Single-degree of freedom
941   systems., J. Earthq. Eng. 7 (2003) 97–118.
942 [25] T.L. Karavasilis, C.-Y. Seo, Seismic structural and non-structural performance
943   evaluation of highly damped self-centering and conventional systems, Eng. Struct. 33
944   (2011) 2248–2258. doi:10.1016/j.engstruct.2011.04.001.
945 [26] G.P. Cimellaro, Simultaneous stiffness–damping optimization of structures with respect
946   to acceleration, displacement and base shear, Eng. Struct. 29 (2007) 2853–2870.
947   doi:10.1016/j.engstruct.2007.01.001.
948 [27] C.-C. Chou, J.-H. Chen, Analytical model validation and influence of column bases for
949   seismic responses of steel post-tensioned self-centering MRF systems, Eng. Struct. 33
950   (2011) 2628–2643. doi:10.1016/j.engstruct.2011.05.011.
951 [28] BS EN 1998-3, Eurocode 8 : Design of structures for earthquake resistance — Part 3:
952   Assessment and retrofitting of buildings., 2005.
953 [29] V.C. Kamperidis, T.L. Karavasilis, G. Vasdravellis, Self-centering steel column base
954   with metallic energy dissipation devices, J. Constr. Steel Res. 149 (2018) 14–30.
955   doi:10.1016/j.jcsr.2018.06.027.
956 [30] H. Chi, J. Liu, Seismic behavior of post-tensioned column base for steel self-centering
957   moment resisting frame, J. Constr. Steel Res. 78 (2012) 117–130.
958   doi:10.1016/j.jcsr.2012.07.005.
959 [31] X.-T. Wang, C.-D. Xie, L.-H. Lin, J. Li, Seismic behavior of self-centering concrete-
960   filled square steel tubular (CFST) Column Base, J. Constr. Steel Res. 156 (2019) 75–85.
961   doi:https://doi.org/10.1016/j.jcsr.2019.01.025.
962 [32] M. Latour, G. Rizzano, A. Santiago, L. Simões da Silva, Experimental response of a
963   low-yielding, self-centering, rocking column base joint with friction dampers, Soil Dyn.
964   Earthq. Eng. 116 (2019) 580–592. doi:https://doi.org/10.1016/j.soildyn.2018.10.011.
965 [33] B. Wang, S. Zhu, C.-X. Qiu, H. Jin, High-performance self-centering steel columns with
966   shape memory alloy bolts: Design procedure and experimental evaluation, Eng. Struct.
967   182 (2019) 446–458. doi:https://doi.org/10.1016/j.engstruct.2018.12.077.
968 [34] FEMA, FEMA P-58-1 Seismic performance assessment of buildings - Volume 1 -
969   Methodology (2nd Edition), Washington, DC, USA, 2018.
970   https://www.fema.gov/media-library/assets/documents/90380.
971 [35] A.S. Tzimas, G.S. Kamaris, T.L. Karavasilis, C. Galasso, Collapse risk and residual drift

972 performance of steel buildings using post-tensioned MRFs and viscous dampers in near-
973 fault regions, Bull. Earthq. Eng. 14 (2016) 1643–1662. doi:10.1007/s10518-016-9898-
974 3.

975 [36] A.I. Dimopoulos, T.L. Karavasilis, G. Vasdravellis, B. Uy, Seismic design, modelling
976 and assessment of self-centering steel frames using post-tensioned connections with web
977 hourglass shape pins, Bull. Earthq. Eng. 11 (2013) 1797–1816. doi:10.1007/s10518-
978 013-9437-4.

979 [37] ASTM, ASTM A416/A416M-05, Standard Specification for Steel Strand, Uncoated
980 Seven-Wire for Prestressed Concrete, West Conshohocken, PA, USA, 2005.

981 [38] T.L. Bruce, M.R. Eatherton, Behavior of Post-Tensioning Strand Systems Subjected to
982 Inelastic Cyclic Loading, J. Struct. Eng. 142 (2016) 04016067.
983 doi:10.1061/(ASCE)ST.1943-541X.0001503.

984 [39] P. Sideris, A.J. Aref, A. Filiatrault, Effects of anchorage hardware on the cyclic tensile
985 response of unbonded monostrands, PCI J. 59 (2014) 60–77.
986 doi:10.15554/pcij.06012014.60.77.

987 [40] G.A. MacRae, C.R. Urmson, W.R. Walpole, P. Moss, K. Hyde, C. Clifton, Axial
988 shortening of steel columns in buildings subjected to earthquakes, Bull. New Zeal. Soc.
989 Earthq. Eng. 42 (2009) 275–287.

990 [41] R. Vargas, M. Bruneau, Analytical Response and Design of Buildings with Metallic
991 Structural Fuses. I, J. Struct. Eng. 135 (2009) 386–93. doi:10.1061/(ASCE)0733-
992 9445(2009)135:4(386).

993 [42] Y.-C. Lin, R. Sause, J.M. Ricles, Seismic Performance of a Large-Scale Steel Self-
994 Centering Moment-Resisting Frame: MCE Hybrid Simulations and Quasi-Static
995 Pushover Tests, J. Struct. Eng. 139 (2013) 1227–1236. doi:10.1061/(ASCE)ST.1943-
996 541X.0000661.

997 [43] T.C. Steele, L.D.A. Wiebe, Collapse risk of controlled rocking steel braced frames with
998 different post-tensioning and energy dissipation designs, Earthq. Eng. Struct. Dyn.
999 (2017). doi:10.1002/eqe.2892.

1000 [44] BS EN 1993-1-1, Eurocode 3: Design of steel structures - Part 1-1: General rules and
1001 rules for steel buildings, United Kingdom, 2009.

1002 [45] BS EN 1993-1-8, Eurocode 3 : Design of steel structures — Part 1-8 : Design of joints,
1003 United Kingdom, 2010.

1004 [46] L. Wiebe, C. Christopoulos, Performance-Based Seismic Design of Controlled Rocking
1005 Steel Braced Frames. I: Methodological Framework and Design of Base Rocking Joint,
1006 J. Struct. Eng. 141 (2015). doi:10.1061/(ASCE)ST.1943-541X.0001202.

1007 [47] G. Vasdravellis, T.L. Karavasilis, B. Uy, Finite element models and cyclic behavior of
1008 self-centering steel post-tensioned connections with web hourglass pins, Eng. Struct. 52
1009 (2013) 1–16. doi:http://dx.doi.org/10.1016/j.engstruct.2013.02.005.

1010 [48] U. of C. Pacific Earthquake Engineering Research Center (PEER), OpenSees, (2015).
1011 http://opensees.berkeley.edu.

1012 [49] M.H. Scott, G.L. Fenves, Plastic hinge integration methods for force–based beam-
1013 column elements, J. Struct. Eng. 132 (2006) 244–252.

1014 [50] D.G. Lignos, H. Krawinkler, Deterioration Modeling of Steel Components in Support
1015 of Collapse Prediction of Steel Moment Frames under Earthquake Loading, J. Struct.
1016 Eng. 137 (2011) 1291–1302. doi:10.1061/(ASCE)ST.1943-541X.0000376.

1017 [51] M. Hamidia, A. Filiatrault, A.J. Aref, Simplified seismic sidesway collapse analysis of
1018 frame buildings, Earthq. Eng. Struct. Dyn. 43 (2014) 429–448. doi:10.1002/eqe.2353.

1019 [52] H. Krawinkler, Shear in Beam-Column Joints in Seismic Design of Frames, Eng. J. 15
1020 (1978).

1021 [53] C.C. Chou, K.C. Tsai, W.C. Yang, Self-centering steel connections with steel bars and

1022   a discontinuous composite slab, Earthq. Eng. Struct. Dyn. 38 (2009) 403–422.
1023   doi:10.1002/eqe.856.

1024 [54] G. Vasdravellis, M. Baiguera, D. Al-Sammaraie, Robustness assessment of a steel self-
1025   centering moment-resisting frame under column loss, J. Constr. Steel Res. 141 (2018)
1026   36–49. doi:10.1016/j.jcsr.2017.11.004.

1027 [55] M. Bruneau, C.-M. Uang, R. Sabelli, Ductile design of steel structures, Second Edi,
1028   McGraw-Hill Education, 2011.

1029 [56] P. Uriz, Towards Earthquake Resistant Design of Concentrically Braced Steel
1030   Structures, University of California, Berkeley, USA, 2005.

1031 [57] VSL International Ltd, Post-tensioning, stay cables & construction methods, Prod.
1032   Broch. VSL STRAND POST-TENSIONING Syst. (2013). www.vsl.com.

1033 [58] M. Baiguera, G. Vasdravellis, T.L. Karavasilis, Ultralow Cycle Fatigue Tests and
1034   Fracture Prediction Models for Duplex Stainless-Steel Devices of High Seismic
1035   Performance Braced Frames, J. Struct. Eng. 145 (2019) 04018230. doi:10.1061/(ASCE)
1036   ST.1943-541X.0002243.

1037 [59] FEMA, Quantification of building seismic performance factors (FEMA P695) (ATC-63
1038   Project), USA, 2009. https://www.fema.gov/media-library-data/20130726-1716-25045-
1039   9655/fema_p695.pdf.

1040 [60] ASCE/SEI, Seismic rehabilitation of existing buildings (ASCE/SEI 41-06), U.S.A.,
1041   2007.

1042 [61] L.T. Kibriya, C. Málaga-Chuquitaypea, M.M. Kashani, N.A. Alexander, Nonlinear
1043   dynamics of self-centring rocking steel frames using finite element models, Soil Dyn.
1044   Earthq. Eng. 1115 (2018) 826–37. doi:https://doi.org/10.1016/j.soildyn.2018.09.036.

1045 [62] J. McCormick, H. Aburano, M. Ikenaga, M. Nakashima, Permissible Residual
1046   Deformation Levels for Building Structures Considering both Safety and Human
1047   Elements, in: 14th World Conf. Earthq. Eng. Oct. 12-17, China Earthquake
1048   Administration Ministry of Construction, Beijing, China, 2008.

1049 [63] D. Vamvatsikos, C.A. Cornell, Incremental dynamic analysis, Earthq. Eng. Struct. Dyn.
1050   31 (2002) 491–514. doi:10.1002/eqe.141.

1051 [64] C.Y. Seo, T.L. Karavasilis, J.M. Ricles, R. Sause, Seismic performance and probabilistic
1052   collapse resistance assessment of steel moment resisting frames with fluid viscous
1053   dampers, Earthq. Eng. Struct. Dyn. 43 (2014) 2059–2216. doi:10.1002/eqe.2440.

1054 [65] J.W. Baker, C.A. Cornell, Spectral shape, epsilon and record selection, Earthq. Eng.
1055   Struct. Dyn. 35 (2006) 1077–95. doi:10.1002/eqe.571.

1056